Combining CRISPR/Cas9 and brain imaging: from genes to proteins to networks

Sabina Marciano[1], Tudor Mihai Ionescu[1], Ran Sing Saw[1], Rachel Y. Cheong[2], Deniz Kirik[2], Andreas Maurer[1], Bernd Pichler[1], Kristina Herfert[1]*

[1]Werner Siemens Imaging Center, Department of Preclinical Imaging and Radiopharmacy, Eberhard Karls University Tuebingen, Germany

[2]Brain Repair and Imaging in Neural Systems, Department of Experimental Medical Science, Lund University, Sweden

*Corresponding author: Prof. Dr. Kristina Herfert (kristina.herfert@med.uni-tuebingen.de)

Address: Roentgenweg 13, 72076 Tuebingen, Germany, Tel: +49 7071 29 87680

Abstract

Understanding how functional connections between brain regions are arranged and influenced by genes, in the healthy and diseased states, is a major goal in neuroscience. Functional connectivity alterations are linked to molecular changes in several neurodegenerative disorders and could serve as early markers of pathology. Yet, the underlying molecular signatures driving the functional alterations remain largely unknown. Here, we combine CRISPR/Cas9 gene-editing with *in vivo* positron emission tomography (PET) and functional magnetic resonance imaging (fMRI) to investigate the direct link between genes, proteins, and the brain connectome. The extensive knowledge of the *Slc18a2* gene encoding the vesicular monoamine transporter (VMAT2), involved in the storage and release of dopamine, makes it an excellent basis for studying the gene networks relationships. We edited *Slc18a2* into the substantia nigra pars compacta of adult rats and used *in vivo* molecular imaging, behavioral, histological, and biochemical assessments to characterize the CRISPR/Cas9-mediated VMAT2 knockdown. Simultaneous PET/fMRI was performed to inspect the functional brain adaptations, beyond the predicted dopaminergic changes. Further, [^{11}C]flumazenil PET was carried out to investigate the dopamine-GABA interplay. We found a regional increase in postsynaptic dopamine receptor availability, preceded by a reorganization of brain networks that adapt to reduced dopamine transmission states by becoming functionally connected and organized. The hyperconnectivity within and between brain networks spreads from the contralateral thalamus and prefrontal cortical regions to the striata and hippocampi. Additionally, impaired striatal dopamine release reduces GABA-A receptor availability, complementing the increased synchrony and functional connectivity between networks observed at rest. Our study reveals that recruiting different brain networks may be an early response to the dopaminergic dysfunction preceding neuronal cell loss, postsynaptic changes, and motor impairment in neurodegenerative disorders such as Parkinson´s disease. We anticipate our combinatorial approach to be a starting point to investigate the impact of

specific genes on brain molecular and functional dynamics, aiding in the identification of early neurobiological markers and promising therapeutic interventions.

Keywords

CRISPR/Cas9, Functional Connectivity, Dopamine, VMAT2, D2 receptor, [^{11}C]raclopride, PET/fMRI.

Introduction

The brain is a network of spatially distributed but functionally and structurally interconnected regions that exhibit correlated activity over time. They communicate with each other via highly specialized neuronal connections and are organized in neuronal circuits and networks. Understanding how functional connections between regions are arranged in the healthy and diseased brain is therefore of great interest.

Resting-state functional magnetic resonance imaging (rs-fMRI) has enabled neuroscientists to delineate the level of functional communication between anatomically separated regions [1]. Rs-fMRI measures the resting-state functional connectivity (rs-FC) at high spatial and temporal resolutions based on spontaneous fluctuations of the blood oxygen level-dependent (BOLD) signal at rest, which indirectly detects neuronal activity via hemodynamic coupling [2]. Using rs-fMRI several brain resting-state networks in humans and rodents have been identified, such as the default mode and sensorimotor networks (DMN, SMN) [3-9]. Alterations of these networks are linked to neurological diseases [10, 11], and may serve as early therapeutic and diagnostic biomarkers. However, the molecular signatures related to the functional alterations in disease remain largely unknown.

Positron emission tomography (PET) provides a non-invasive tool to indirectly measure molecular changes in the brain with high specificity and sensitivity. One well-characterized example is the radioligand [^{11}C]raclopride, a widely used D2/D3 receptor antagonist enabling the non-invasive determination of dopamine release and availability [12-14].

PET in combination with BOLD-fMRI has the great potential to investigate the molecular substrate of brain functional connectivity (FC), enabling the direct spatial and temporal correlation of both measurements [15-21]. In this context, we have recently shown that rs-FC is modulated by intrinsic serotonin transporter and D2/3 receptor occupancy in rats [22].

78 Insights into functional brain circuits and their relationships to individual phenotypes can be
79 gained by genetic manipulations of neuronal subtypes [23]. Genome-engineering methodologies
80 based on clustered regularly interspaced short palindromic repeats (CRISPR)/associated RNA-
81 guided endonuclease (Cas9) represent a promising approach to unveil the influence of genes on
82 brain circuits. CRISPR/Cas9 has enabled researchers to interrogate the mammalian DNA in a
83 precise yet simple manner [24, 25] in several species [26-31], by editing single or multiple
84 genomic loci *in vitro* and *in vivo* [25, 32, 33]. However, one great hurdle is the brain delivery,
85 which must comply with effective nuclear access, while minimizing immunogenic reactions and
86 off-target editing [34]. Despite these limitations, the potential of CRISPR/Cas9 is continuously
87 expanding with novel nuclease variants being exploited [35-37]. Derived from *Staphylococcus*
88 *aureus*, SaCas9 overcomes the packaging constraints of adeno-associated viral vectors (AAVs),
89 allowing efficient CRISPR/Cas9 brain transfer [38-42].

90 Here, we use an AAV-based CRISPR/SaCas9 gene-editing approach to knock down the *Slc18a2*
91 gene encoding the vesicular monoamine transporter 2 (VMAT2), a key protein involved in the
92 storage and release of dopamine in the brain [43]. The extensive knowledge on *Slc18a2* makes it
93 an excellent basis for studying the gene networks relationships. We characterize the VMAT2-
94 mediated dopamine signaling using *in vivo* molecular imaging, behavioral, histological, and
95 biochemical assessments. We investigate the impact of impaired VMAT2-dependent dopamine
96 neurotransmission on the DMN and SMN using a simultaneous [^{11}C]raclopride-PET/fMRI
97 protocol. Further, we dig into the dopamine-GABA interplay using [^{11}C]flumazenil PET. Our
98 results reveal that CRISPR/SaCas9-induced synaptic dysfunction prompts early network
99 changes, preceding motor and molecular alterations, including a regional increase in postsynaptic
100 dopamine receptor availability. We identify a pattern of asymmetric hyperconnectivity, and
101 internetwork synchronization, spreading from the contralateral thalamus (SMN), and prefrontal
102 cortical regions (DMN) to the striata and hippocampi, complemented by a reduced GABA-A
103 receptor availability.

104 Our findings illustrate the ability of the brain to recruit different brain networks and functionally
105 compensate for the dopaminergic dysfunction prior to neuronal cell loss, postsynaptic changes,
106 and motor impairment.

107

108 ## Results

109 ### *In vitro* validation of CRISPR/SaCas9-induced VMAT2 knockdown in rat primary cortical
110 neurons

111 To evaluate the efficiency of the AAV-based CRISPR/SaCas9 VMAT2 knockdown in rat primary
112 neurons, we designed AAV-SaCas9 and AAV-sgRNA targeting the first exon of the bacterial *lacZ*
113 gene (control) or the second exon of the *Slc18a2* gene (Fig. 1a) (sgRNAs sequences are
114 reported in Table 1). Seven days post-transduction, the protein expression level and mutation
115 rate of the harvested genomic DNA were inspected by immunofluorescence and surveyor assay
116 (Fig. 1b). Immunofluorescence indicated a clear reduction of VMAT2 protein expression in
117 neurons transduced with AAV-SaCas9 and AAV-sgRNA-*Slc18a2* (Fig. 1c). We observed 20%
118 editing for the digested DNA from neurons transduced with vectors for SaCas9 and sgRNA-
119 *Slc18a2* (Supplementary Fig.1).

120

121 ### CRISPR/SaCas9-induced VMAT2 knockdown elicits postsynaptic changes but no nerve
122 terminal loss or neuroinflammation in the adult rat brain

123 To test the *in vivo* efficiency of the CRISPR/SaCas9 gene-editing, we expressed SaCas9 and
124 sgRNA targeting *Slc18a2* to knock down the VMAT2, or targeting *lacZ* as control, by AAV-
125 mediated gene transfer into the right substantia nigra pars compacta (SNc). DPBS was injected
126 into the left SNc. [^{11}C]Dihydrotetrabenazine (DTBZ) PET imaging was performed 8 – 10 weeks
127 post-injection to quantify VMAT2 expression in the striatum (Fig. 2a).

128 [^{11}C]DTBZ binding was decreased by 30% in the right striatum of rats where the VMAT2 was
129 knocked down in comparison to the contralateral striatum. No changes of [^{11}C]DTBZ binding were
130 observed in the contralateral striatum, as [^{11}C]DTBZ binding did not differ between the left
131 striatum of rats injected with sgRNA targeting *lacZ* and rats injected with sgRNA targeting
132 *Slc18a2* (Fig. 2b,c).
133 We further evaluated changes of dopamine availability in the striatum using [^{11}C]raclopride, which
134 competes with dopamine for the same binding site at the D2 receptor (D2R) [13]. After
135 12 – 14 weeks following CRISPR/SaCas9-induced VMAT2 knockdown in nigrostriatal neurons,
136 we observed 17% increased binding of [^{11}C]raclopride in the right striatum of VMAT2 knockdown
137 rats and no changes in control rats (Fig. 2b,c), indicating a reduction of synaptic dopamine levels
138 and/or compensatory changes of D2R expression at postsynaptic medium spiny neurons. A
139 larger VMAT2 knockdown led to lower dopamine levels in the striatum and thus to higher D2R
140 binding (Fig. 2d). To explore the threshold at which the observed postsynaptic changes occur, we
141 calculated the [^{11}C]raclopride/[^{11}C]DTBZ binding ratio for the right and left striatum. The ratio
142 remained close to 1 in the DPBS-injected striatum and control rats, indicating no substantial
143 difference between the two hemispheres. In contrast, VMAT2 knockdown rats displayed large
144 [^{11}C]raclopride binding changes when the level of VMAT2 knockdown was ~ 20%. From this
145 point, a prominent increase in D2R binding was observed in the right striatum (Fig. 2e).
146 Therefore, this threshold was set to split the rats into *mild* (< 20%) and *moderate* (≥ 20%).
147 Notably, [^{11}C]raclopride PET imaging was able to discriminate between different degrees of
148 synaptic dysfunction, classified from [^{11}C]DTBZ binding changes (Fig. 2f).
149 We inspected the integrity of dopaminergic nerve terminals and the occurrence of
150 neuroinflammation in the striatum after the CRISPR/SaCas9-induced VMAT2 knockdown.
151 [^{11}C]methylphenidate PET imaging of the dopamine transporter and [^{18}F]GE-180 PET imaging of
152 the translocator protein, which is overexpressed on activated microglia, was performed.

153 CRISPR/SaCas9-induced VMAT2 knockdown did neither alter [^{11}C]methylphenidate binding, nor
154 [^{18}F]GE-180 uptake (Fig. 2b,c).
155
156 **CRISPR/SaCas9-induced VMAT2 knockdown impairs motor function**

157 To explore the motor consequences of the CRISPR/SaCas9-induced VMAT2 knockdown, we
158 performed several behavioral tests (Fig. 3a).
159 We observed a reduction in the locomotor activity of VMAT2 knockdown rats in the open field test
160 (Fig. 3a), but no correlation to VMAT2 expression changes (Δ [^{11}C]DTBZ binding), or dopamine
161 availability (Δ [^{11}C]raclopride binding) (Supplementary Fig. 2a,b).
162 Next, we evaluated the forelimb akinesia using the cylinder test. VMAT2 knockdown rats
163 displayed a preference for the right forepaw, while control rats equivalently used their right and
164 left forepaw (Fig. 3c). Paw use alterations correlated highly with VMAT2 knockdown (Δ [^{11}C]DTBZ
165 binding), and dopamine availability (Δ [^{11}C]raclopride binding) (Fig. 3d,e).
166 To further examine differences in motor function, coordination, and balance, rats underwent the
167 beam walk test. VMAT2 knockdown rats stumbled with higher frequency to the left side, while
168 control rats displayed equal chances to slip in each direction (Fig. 3f). However, no correlations
169 between gait alterations and VMAT2 knockdown (Δ [^{11}C]DTBZ binding), or dopamine availability
170 (Δ [^{11}C]raclopride binding) were found (Supplementary Fig. 2c,d).
171 As previous studies suggest that body weight changes reflect striatal dopamine depletion [44], we
172 inspected the impact of the VMAT2 knockdown on the rats' body weight gain. VMAT2 knockdown
173 rats exhibited a 30% reduction in their gained weight over a period of 14 weeks, compared with
174 controls (Fig. 3g). Body weight gain correlated with changes in VMAT2 expression (Δ [^{11}C]DTBZ
175 binding), and dopamine availability (Δ [^{11}C]raclopride binding) (Fig. 3h,i).
176 To assess the rotational behavior, we performed the rotameter test with and without apomorphine
177 administration. In the spontaneous rotation test, VMAT2 knockdown rats displayed a higher
178 number of ipsilateral net turns compared with control rats (Fig. 3j). The number of turns did not

179 correlate with VMAT2 expression changes (Δ [^{11}C]DTBZ binding), and changes in dopamine
180 availability (Δ [^{11}C]raclopride binding) (Supplementary Fig. 2e,f). Apomorphine-induced rotations
181 to the contralateral side were higher in VMAT2 knockdown rats compared with control rats (Fig.
182 3k), and correlated with changes in VMAT2 expression (Δ [^{11}C]DTBZ binding) and dopamine
183 availability (Δ [^{11}C]raclopride binding) (Fig. 3l,m).
184

185 ***Ex vivo* validation of the CRISPR/SaCas9-induced VMAT2 knockdown**

186 Using immunofluorescence, we confirmed the concomitant expression of SaCas9 and *Slc18a2*–
187 targeting sgRNA 19 weeks post-transduction, and a corresponding decrease of VMAT2
188 expression in the SNc of the VMAT2 knockdown group (Fig. 4b).
189 Immunohistochemistry revealed no changes in tyrosine hydroxylase (TH) expression levels in
190 striatum and SN in both groups (Fig. 4c,d), and confirmed the reduction of VMAT2 expression in
191 the right striatum and SN in the knockdown group (Fig. 4e).
192 Biochemical analysis showed a large reduction of dopamine, paralleled by an increased ratio of
193 metabolites (DOPAC, HVA) to dopamine, in the right striatum of VMAT2 knockdown rats (Fig.
194 4f,g). The reduced dopamine content correlated with the *in vivo* VMAT2 expression (Δ [^{11}C]DTBZ
195 BP_{ND}) and postsynaptic changes (Δ [^{11}C]RAC BP_{ND}) (Fig. 4h,i). Additionally, serotonin was
196 unchanged in the striata of VMAT2 knockdown and control rats, suggesting dopamine
197 nigrostriatal pathway specificity (Fig. 4j) (Metabolites' and neurotransmitters' striatal levels are
198 reported in Table 3).
199

200 **Increased resting-state functional connectivity after CRISPR/SaCas9-induced VMAT2**
201 **knockdown**

202 As multiple lines of evidence suggest a broader role of dopamine in the dynamic reconfiguration
203 of brain networks [17, 45, 46], we next investigated the impact of unilateral dopamine depletion
204 on brain rs-FC. A second cohort of rats underwent longitudinal simultaneous [^{11}C]raclopride-

205 PET/BOLD-fMRI scans at baseline and 8 - 14 weeks after CRISPR/SaCas9-induced VMAT2
206 knockdown (Fig. 5a). [^{11}C]DTBZ PET scans and behavioral analysis confirmed previous findings
207 in the first cohort, that is, an efficient depletion of the VMAT2 (20% decrease of [^{11}C]DTBZ
208 binding) (Supplementary Fig. 3a), paralleled by motor disturbances in the cylinder test
209 (Supplementary Fig. 3e-g). In line with the findings of cohort 1, dopamine availability was
210 decreased (10% increase in [^{11}C]raclopride binding) and correlated to the extent of the VMAT2
211 knockdown (Supplementary Fig. 3b,c). An increase in D2R binding was observed in the right
212 striatum when the level of VMAT2 knockdown reached ~ 20% (Supplementary Fig. 3d), enabling
213 a subdivision into *mild* (< 20%) and *moderate* rats (≥ 20%).
214 We next assessed the occurrence of rs-FC changes in DMN and SMN. Our analysis focused on
215 identifying early biomarkers of *mild* dysfunction and patterns of spreading of synaptic dysfunction.
216 Figure 5b,c illustrates intraregional rs-FC group-level correlation matrices at baseline and after
217 VMAT2 knockdown in *mild* and *moderate* rats for the DMN and SMN, respectively. We observed
218 within-network rs-FC changes in rats with *moderate* VMAT2 knockdown, in both DMN and SMN.
219 Rats of the *mild* knockdown group revealed rs-FC changes up to 20%, in prefrontal cortical
220 regions of the DMN, and between the left thalamus (Th) and somatosensory cortex (SC) in the
221 SMN. However, these data need to be carefully interpreted as they did not survive a more
222 stringent *P* value selection (**P*< 0.01) (Supplementary Fig.4a,b) (*P* values are reported in
223 Supplementary Tables 1,3).
224 Rats with *moderate* VMAT2 knockdown exhibited a 60% increase in rs-FC within the right medial
225 prefrontal cortex (mPFC) and the right and left hippocampus (Hipp) (Fig. 5b) (*P* values are
226 reported in Supplementary Table 2).
227 FC increase between the left thalamus and somatosensory cortex in the SMN doubled to 34% in
228 rats with *moderate* VMAT2 knockdown and extended throughout the left and right thalamus and
229 striatum (STR), respectively (Fig. 5c) (*P* values are reported in Supplementary Table 4).

230 Moreover, we inspected rs-FC changes between the DMN and SMN at baseline and after the
231 CRISPR/SaCas9-induced VMAT2 knockdown.
232 Figure 5d illustrates internetwork rs-FC correlation matrices in rats with *mild* (left panel) and
233 *moderate* (right panel) VMAT2 knockdown. Brain graphs display the nodes and edges (raw
234 values) that demonstrated internetwork rs-FC changes to baseline (%). Strikingly, large
235 alterations between DMN and SMN were already observable in the *mild* VMAT2 knockdown
236 group. Rats presented opposite rs-FC changes between regions of the anterior/posterior DMN
237 and the SMN, compared with baseline. A 30 to 60% increase in rs-FC was observed between
238 regions of the anterior DMN and the SMN. Specifically, rs-FC increased between the right
239 orbitofrontal cortex (OFC) and striatum bilaterally and the contralateral somatosensory cortex,
240 and between the contralateral orbitofrontal cortex and striatum. Instead, a 20% decrease in rs-FC
241 was found between regions of the posterior DMN and the SMN. Specifically, rs-FC decreased
242 between the left retrosplenial cortex (RSC) and right somatosensory cortex (Fig. 5d, left panel) (*P*
243 values are reported in Supplementary Table 5).
244 Rats with a *moderate* VMAT2 knockdown presented increased rs-FC between regions of the
245 anterior/posterior DMN and the SMN, compared with baseline. Of particular note, internetwork rs-
246 FC changes were not found between the regions of the posterior DMN and the SMN that showed
247 decreased rs-FC in rats with *mild* VMAT2 knockdown. Moreover, between-network rs-FC
248 increase extended to other regions. A 60 to 80% increase in rs-FC was found between the medial
249 prefrontal cortex and the right striatum, and the motor (MC) and somatosensory cortex bilaterally.
250 FC increased by more than 20% between the hippocampi and contralateral somatosensory
251 cortex. (Fig. 5d, right panel) (*P* values are reported in Supplementary Table 6). Notably, between-
252 network rs-FC changes did not involve the thalamus, which connectivity was however altered
253 within the SMN.

254 Further, we examined how the rs-FC changes to baseline correlated between the *mild* and
255 *moderate* groups (Supplementary Fig. 5a). Group level intraregional and internetwork rs-FC

256 changes to baseline (%) correlated linearly between the two groups (Supplementary Fig. 5b-d).
257 Node correlation analysis indicated a linear increase in the magnitude of the rs-FC changes to
258 baseline in the hippocampi (Supplementary Fig. 5e), cingulate cortices (Supplementary Fig. 5f),
259 and contralateral, but not ipsilateral, thalamus (Supplementary Fig. 5g). Our data suggest a
260 similarity in the pattern of the intraregional and internetwork rs-FC changes between *mild* and
261 *moderate* VMAT2 knockdown rats and a linear relationship between the magnitude of the rs-FC
262 changes.

263 To complement the results of the intraregional and internetwork rs-FC, we evaluated changes in
264 regional mean connection distances. Network-wise graph theoretical analysis on node level was
265 paralleled by whole-brain connection-wise analysis to identify the nodes that were significantly
266 altered in rats with *mild* and *moderate* VMAT2 knockdown, compared with baseline, for the DMN
267 (Supplementary Fig. 6a,b) and SMN (Supplementary Fig. 6c,d). Briefly, the network organization
268 did not change in rats with *mild* VMAT2 knockdown, compared with baseline, as changes in the
269 global mean connection distance were not found in DMN (Supplementary Fig. 6a) nor SMN
270 (Supplementary Fig. 6c). Interestingly, in rats with *moderate* VMAT2 knockdown network
271 organization changes did not influence regions of the DMN (Supplementary Fig. 6b), but occurred
272 in the contralateral striatum and thalamus (Supplementary Fig. 6d) (*P* values are reported in
273 Supplementary Table 7).
274 Collectively, rs-FC results highlight lateralized effects in the SMN, as opposed to the symmetric
275 recruitment of DMN regions.
276

277 **CRISPR/SaCas9-induced VMAT2 knockdown alters GABA signaling**

278 Besides dopamine, dopaminergic neurons co-release GABA via the VMAT2 [47, 48]. To
279 investigate if GABA neurotransmission is altered following the VMAT2 knockdown, we performed
280 additional [^{11}C]flumazenil PET scans 10 – 12 weeks after the CRISPR/Cas9-editing, and

281 quantified the GABA-A binding in regions of the DMN and SMN (Fig. 6). In *mild* VMAT2
282 knockdown rats, we observed a decrease of [^{11}C]flumazenil binding in the ipsilateral parietal
283 cortex (PaC) (14%), hippocampus (4%), and somatosensory cortex (9%) (Fig. 6a,b). In *moderate*
284 VMAT2 knockdown rats we observed a decrease of [^{11}C]flumazenil binding in the ipsilateral
285 parietal cortex (11%), and somatosensory cortex (6%) (Fig. 6a,c). Our data indicate that
286 [^{11}C]flumazenil binding was altered regardless of the VMAT2 knockdown extent. This was further
287 evidenced by the lack of correlation between [^{11}C]DTBZ and [^{11}C]flumazenil binding changes in
288 the target regions (linear regression data not shown).
289

290 **Discussion**

291 Here, we show the potential of combining CRISPR/Cas9 gene-editing with molecular and
292 functional brain imaging to identify early adaptations of brain circuits in response to targeted gene
293 and protein modulations. Using CRISPR/SaCas9, we knocked down the *Slc18a2* gene, encoding
294 the VMAT2, which plays a key role in the storage and release of dopamine in response to
295 neuronal activity [43]. The CRISPR-mediated knockdown allowed us to investigate the VMAT2-
296 dependent dopamine signaling in the striatum, while structurally preserving neuronal integrity.
297 [^{18}F]GE-180 results suggest that glial activation is not the source of dopaminergic synaptic
298 dysfunction, and exclude the occurrence of inflammatory responses arising from the surgical
299 procedure and the chosen AAV-serotype, which could influence our readout, in line with recent
300 reports [49]. Our data reveal that the targeted gene knockdown in the SNc leads to an expected
301 reduction of dopamine release in the striatum, paralleled by [^{11}C]raclopride binding changes. It is
302 conceivable that the observed postsynaptic changes are the result of an increase in binding due
303 to the reduced dopamine concentration in the striatum. Yet, several studies have revised this
304 notion [50, 51]. In this regard, our results of the drug-evoked rotational behavior are in better
305 agreement with a D2R compensatory upregulation. Indeed, supersensitivity to apomorphine in
306 rats with nigrostriatal lesions or VMAT2 knockout is accompanied by an increase in striatal D2R

307 binding sites, but no change in affinity [52-57]. Further, the observed striatal increase in
308 [^{11}C]raclopride binding is independent of presynaptic nerve terminal loss and occurs in response
309 to a ~ 20% decrease of [^{11}C]DTBZ binding. This confirms, in line with our [^{11}C]methylphenidate
310 results, that [^{11}C]raclopride can be used to delineate postsynaptic changes in the absence of
311 dopamine transporter-mediated compensation, triggered by neuronal loss. Accordingly, increased
312 [^{11}C]raclopride binding is observed in the early but not later stages of Parkinson`s disease [58],
313 characterized by severe neuronal cell loss, and dopamine transporter changes (> 50%) [59].
314 Consistently, rats with severe denervation (> 75%) present earlier mitigation by the dopamine
315 transporter, followed by D2R binding changes [60]. Hence, with our method, it is feasible to study
316 the consequences of synaptic dopamine dysfunction without compensations triggered by
317 neuronal cell loss. Moreover, the observed [^{11}C]raclopride and [^{11}C]DTBZ correlations to the
318 motor behavior highlight that [^{11}C]raclopride binding remains at control levels as long as synaptic
319 dopamine levels are sufficient to maintain adequate motor function. Motor disturbances strongly
320 correlate to pre and postsynaptic changes if movements of the forelimbs, but not whole-body, are
321 considered, in agreement with earlier observations in dopamine-depleted rats [44]. Depletion of
322 VMAT2 resulted in reduced dopamine tissue levels in the ipsilateral striatum, nicely merging with
323 the *in vivo* data. Moreover, metabolite analysis suggested that due to the lack of VMAT2-
324 mediated storage in presynaptic vesicles, dopamine is quickly converted. The increased
325 metabolism might as well be a possible compensatory mechanism consequent to the VMAT2
326 knockdown, reflecting actions that residual nigrostriatal neurons undertake to maintain dopamine
327 homeostasis, as already speculated by others [53, 61].
328 To elucidate the role of VMAT2 in locomotion, reward, and Parkinson`s disease, several
329 investigators have deleted its coding gene in mice [62-65]. Besides the costly and time-
330 consuming breeding, the gene knockout was not selective for dopaminergic neurons, resulting in
331 the appearance of anxiety and depressive behavior phenotypes [66]. CRISPR/Cas9-editing
332 overcomes these limitations, allowing gene-editing in adult and aged animals and avoiding

333 compensatory changes occurring at early developmental stages. Since its discovery, only two
334 studies have successfully applied CRISPR/Cas9 in the rat brain [40, 67], where gene-editing has
335 been difficult to adapt. Rats are particularly advantageous for imaging studies due to the larger
336 brain size and limited spatial resolution and sensitivity of preclinical scanners [68]. Here, by
337 inducing a *mild* to *moderate* gene knockdown, we could investigate early to late resting-state
338 brain network adaptations prompted by presynaptic dysfunction. We show that the selective
339 impairment of presynaptic dopamine storage and release is followed by rs-FC alterations within
340 and between the DMN and SMN. Our results confirm previous findings that the DMN, associated
341 with ideation and mind wandering [69], and the SMN, involved in sensory processing and motor
342 function [70], do not function in isolation from each other, but rather synchronize [71]. The
343 observed internetwork synchronization may reflect compensatory brain reorganization, as already
344 speculated by others [72, 73]. We also identified enhanced intranetwork rs-FC in the DMN and
345 SMN. Rs-FC changes were observed in prefrontal cortical regions, hippocampus, thalamus, and
346 striatum. Our data parallel previous findings of cortico-striato-thalamic hyperconnectivity in
347 decreased dopamine transmission states [74-77]. In line, increased synchronous neural
348 oscillatory activity and functional coupling in the basal ganglia and its associated networks have
349 been observed in Parkinson`s disease [78-83]. The increase of cortico-striatal FC could in part be
350 due to dysfunctions of multiple tonic inhibitory gate actions of D2R [84]. Increased FC across the
351 thalamus and prefrontal cortex has been reported in drug-treated Parkinson`s disease patients
352 [85, 86], potentially indicating functional compensation, as the brain recruits additional anatomical
353 areas to aid in restoring cognitive processes. This might as well explain the engagement of the
354 hippocampus, functionally connected with DMN cortical regions [87, 88]. In this regard, research
355 has shown that the hyperconnectivity of brain circuits is a common response to neurological
356 dysfunction, and may reflect a protective mechanism to maintain normal brain functioning [89].
357 Such a mechanism has been proposed in Parkinson`s disease, mild cognitive impairment, and
358 Alzheimer's disease [90-93]. Collectively, our findings support this model and indicate a

359 reorganization of brain networks that adapt to the synaptic dysfunction through enhanced
360 interregional synchrony. Recruiting alternative brain regions may be an early response to the
361 dysfunction preceding neuronal cell loss and motor impairment. Interestingly, brain connectome
362 adaptations occurred symmetrically in the DMN but were more weighted towards the contralateral
363 hemisphere in the SMN.
364 Besides dopamine, dopaminergic neurons co-release GABA via the VMAT2. This hints towards
365 reduced GABA following the VMAT2 knockdown, and consequent imbalance in downstream
366 striatal projection neurons of the direct and indirect pathway [47, 48, 94]. GABA regulates the
367 inhibitory neurotransmission in various brain areas through GABA-A receptors [95]. We
368 hypothesize that decreased binding to the GABA-A receptors may be consistent with loss of
369 inhibitory tone in multiple cortical areas, reflected by our [^{11}C]flumazenil PET data, resulting in
370 increased localized brain connectivity, reflected in the fMRI signal. The suppression of the
371 GABAergic feedback circuit, mediated by D2R and external globus pallidus neurons [84],
372 complements the observed elevation in neuronal synchronicity. Our postulation is in line with
373 earlier findings of an inverse correlation of GABA with rs-FC in DMN [96] and with a putative role
374 of loss of inhibitory tone in hyperconnectivity [97]. Interestingly, our [^{11}C]flumazenil PET data did
375 not reveal changes in GABA-A expression in the striatum. Instead, we observed a significant
376 decrease in the ipsilateral hemisphere of several cortical regions in both *mild* and *moderate* rats,
377 supporting previous findings of GABA modulation of the internetwork FC [98]. Studies report
378 downregulated inhibitory neurotransmission in Parkinson`s disease, where gene expression of
379 GABAergic markers is low in the frontal cortex [99, 100]. Further, inverse correlations between
380 [^{11}C]flumazenil binding and gait disturbances [101], and between GABA concentration in the
381 motor cortex and disease severity have been reported [102]. Moreover, our [^{11}C]flumazenil PET
382 results suggest that GABA neurotransmission is disturbed already at the *mild* stage, indicating its
383 potential role as an early biomarker of dopaminergic presynaptic dysfunction. Of note, the
384 observed changes in GABA-A binding might indicate only an apparent decrease in binding due to

385 the reduced GABA availability, or reflect compensatory adaptation on the contralateral
386 hemisphere. Future research should elucidate these aspects and also perform further
387 investigations on glutamate, due to the crucial role of the excitatory/inhibitory-imbalance in
388 several psychiatric disorders [103].
389
390 **Limitations and general remarks**

391 We knocked down VMAT2 in dopaminergic projection neurons from the SNc to the dorsal
392 striatum. To achieve selective targeting of this neuronal subtype, rat Cre driver lines have been
393 developed [67, 104]. Although all monoamine-releasing neurons express VMAT2, in contrast to
394 other brain regions, SNc neurons are predominantly dopaminergic [105]. Thus, even though we
395 used wild-type rats, we can largely dismiss effects on other monoaminergic neurons, as also
396 indicated by biochemical analysis of serotonin striatal levels.
397 Despite its limited off-target editing [38], undesired targeting of SaCas9 on other genes cannot be
398 fully excluded. Nevertheless, off-target candidates with up to 4 mismatches were screened in the
399 whole genome of *Rattus norvegicus* (http://www.rgenome.net/cas-offinder/), consistently with
400 past reports [40]. To the best of our knowledge, the off-target matches (*Ndrg1*, *RGD1305938*,
401 *Btn2a2*, *AABR07042293.2)* have no effects on VMAT2 function, being involved in cell
402 differentiation, T-cell regulation, and mRNA processing, respectively
403 (https://www.ncbi.nlm.nih.gov/IEB/Research/Acembly/index.html).
404 Another limitation of the study is the relatively small sample size, related to the complex and high-
405 cost procedures involved in the *in vivo* imaging measurements. In addition to this, the intrinsically
406 high intersubject variability in rs-fMRI, and differences in knockdown efficiency contributed to
407 significant variance in our cohorts. Nevertheless, the variability of gene-editing efficiency was in
408 line with previous *in vivo* brain studies [40, 41].
409
410 **Conclusions**

411 This work encourages the combinatorial use of CRISPR/Cas9 and molecular and functional *in*
412 *vivo* brain imaging to achieve selective modulation of genes and understand the related functional
413 adaptations in brain networks, beyond the targeted circuitry.
414 We anticipate our approach to be a starting point to shed the light on the function of specific
415 genes and their encoded proteins on whole-brain connectivity, useful to understand the cellular
416 basis of functional changes, identify early neurobiological markers, and promising therapeutic
417 interventions.
418

419 **Methods**

420 **Animals**

421 Female wild-type Long Evans rats (224 ± 30 g, n = 57) (Charles River Laboratories, Sulzfeld,
422 Germany) were kept on a 12 h day-night cycle at a room temperature of 22 °C and 40 - 60%
423 humidity. Animals received a standard diet and tap water *ad libitum* before and during the
424 experimental period. All animal experiments were performed according to the German Animal
425 Welfare Act and were approved by the local ethical authorities, permit numbers R15/19M,
426 R4/20G.
427

428 **Viral vectors**

429 SgRNAs targeting the second exon of the *Slc18a2* gene and the first exon of the *lacZ* gene were
430 designed based on the PAM sequence of SaCas9 (NNGRRT) (Table 1). SgRNAs were cloned
431 into an AAV-PHP.EB expression vector containing a GFP reporter sequence, driven by the CMV
432 promoter, for the identification of transduced neurons. A second AAV-PHP.EB construct was
433 produced to express SaCas9, flanked by two nuclear localization sequences (NLS) to allow its
434 translocation into the nuclei. The vector expressed the nuclease via the CAG promoter and
435 contains three HA-tags to visualize the targeted neurons (Fig. 1a). Cloning of the sgRNAs,
436 plasmid construction, as well as the production of concentrated and purified AAV-PHP.EB
437 vectors, delivered at a concentration of 10^{13} gc/mL, were carried by SignaGen Laboratories
438 (Frederick, Maryland, USA). A European patent application has been filed for the AAV-PHP.EB
439 vectors and is currently pending.
440 The genomic mutation rate was assessed using a different set of AAVs with AAV2/1 serotype, for
441 a conditional design, kindly provided by Matthias Heidenreich (prev. Zhang lab, Broad Institute of
442 MIT and Harvard, Cambridge, USA).
443

444 **Rat primary cortical neuron culture**

445 Primary cortical neurons were obtained from rat embryos of a pregnant Sprague Dawley rat from
446 embryonic day 18 (E18) (Charles River, Sulzfeld, Germany). Embryos were decapitated and
447 quickly removed from the mother rat. Cortical dissection was performed in ice-cold HBSS
448 (100 mL 10 × HBSS, 870 mL dH_2O, 3.3% 0.3 M HEPES pH 7.3 and 1% pen/strep)
449 (LifeTechnologies, Massachusetts, USA). The obtained tissue was washed three times with
450 10 mL ice-cold HBSS PhenolRed-free (LifeTechnologies, Massachusetts, USA) and then
451 digested at 37 °C for 20 min in 8 mL HBSS with 2.5% trypsin (LifeTechnologies, Massachusetts,
452 USA). Cortices were washed 3 times with 10 mL HBSS containing 3.7% FBS, and then gently
453 triturated in 2 mL HBSS. For the maintenance, neurons were plated on poly-D-lysine-coated 24
454 well plates (BD Biosciences, Heidelberg, Germany) or coverslips (Neuvitro Corporation,
455 Vancouver, USA) at a density of 16×10^4/well, and cultured in Neurobasal media supplemented
456 with 2% 1 × B27, 0.25% Glutamax, 0.125% Glutamate and 1% pen/strep (LifeTechnologies,
457 Massachusetts, USA) for four days. Afterward, for the immunofluorescence, AAVs carrying the
458 expression of the vectors for the SaCas9 and sgRNAs (1:1 ratio), were added to the culture
459 medium at 200,000 MOI (AAV-PHP.EB-sgRNA-*lacZ:* 1.7×10^{12} gc/mL, AVV-PHP.EB-SaCas9:
460 1.4×10^{12} gc/mL, AAV-PHP.EB-sgRNA-*Slc18a2:* 2.1×10^{12} gc/mL, final viral volume
461 37.5 µL/well). For the Surveyor assay, conditional AAVs for SaCas9, sgRNA-*Slc18a2*, Cre-
462 recombinase (AAV2/1, 1:1:0.5 ratio) were used. Neurons were processed 1-week post-viral
463 treatment (Fig. 1b).
464

465 **Surveyor assay**

466 To estimate the VMAT2 knockdown efficiency of the designed sgRNA *in vitro*, we evaluated the
467 presence of genetic deletions in rat primary neurons with the Surveyor assay (Surveyor kit,
468 Integrated DNA Technologies, Coralville, USA). One week following the viral infection, the

469 genomic DNA was extracted using the QuickExtract DNA Extraction solution (Epicentre,
470 Madison, USA), according to the manufacturer´s instructions, and was normalized to 100 ng in
471 dH_2O. 18 - 25 nt primers were designed 200 - 400 bp away from either side of the SaCas9 target
472 site to amplify the loci of interest by touchdown PCR (oligonucleotides used for PCR are provided
473 in Supplementary Table 8). DNA amplification was performed using 0.5 µL Phusion Polymerase
474 (LifeTechologies, Massachusetts, USA), as previously reported [106]. A single band product was
475 visualized on 1.5% agarose gel, isolated, and purified using QIAquick Spin columns (Qiagen,
476 Hilden, Germany), following the supplier's protocol. 400 ng of the purified PCR product were
477 mixed with 2 µL Taq DNA polymerase buffer (LifeTechnologies, Massachusetts, USA) to allow
478 the cross-annealing of the mutated and wild-type sequences. The re-annealing process was
479 conducted at the following cycling conditions: 10 min at 95 °C, 95 °C to 85 °C at -2 °C/s, hold
480 1 min, ramp down to 75 °C at -0.3 °C/s, hold 1 min, and so on until 25 °C temperature was
481 reached. Samples were then stored at 4 °C. This cross-annealing procedure converts the
482 mutations into mismatch duplexes (heteroduplexes), which can be recognized by performing
483 nuclease digestion [107]. We digested the annealed products for 20 min at 42 °C using 2.5 µL
484 $MgCl_2$ (0.15 M), 1 µL Surveyor nuclease, and 1 µL Surveyor enhancer. Digested products were
485 then resolved on a 2.5% agarose gel, stained with 0.01% SYBR Gold DNA (LifeTechnologies,
486 Massachusetts, USA) in 1% TBE buffer. The size of the occurring bands indicated the location of
487 the mutation (expected DNA fragments sizes are provided in Supplementary Table 8). To
488 quantify the knockdown efficiency, the software ImageJ was used. Peak areas of the bands
489 visualized on agarose gel were selected and the percentages of the transduced neurons
490 acquiring the InDel mutation were calculated using the following formula [106]:

491 $$Editing\ (\%) = 100\ \times (1 - \sqrt{\left(1 - \frac{b+c}{a+b+c}\right)}$$

492 where a is the integrated intensity of the undigested PCR product and b and c are the integrated
493 intensities of each cleavage fragment from the digested product.

494

495 **Immunofluorescence of rat primary neurons**

496 Rat primary neurons were processed1-week post-AAV-transduction. Coverslips were washed
497 twice with DPBS and fixed in 4% PFA in DPBS for 15 min at room temperature. Blocking and
498 permeabilization were performed for 30 min in DPBS with 5% donkey serum, 0.5% Triton-X100,
499 and 0.05% BSA. Primary antibody incubation (VMAT2, 1:50, EB06558, Everest Biotech,
500 Ramona, USA, HA-tag: 1:50, 682404, Biolegend, San Diego, USA) was performed for 60 min,
501 followed by Cy3 conjugated secondary antibody incubation (1:250, kindly provided from Birgit
502 Fehrenbacher, Department of Dermatology, University of Tuebingen, Germany). Coverslips were
503 mounted using ProLong Antifade Diamond Medium containing DAPI (LifeTechnologies,
504 Massachusetts, USA), and imaged with a TCS-SP2/Leica DM IRE2 confocal laser scanning
505 microscope. Images were processed with Leica Confocal Software LCS (Version 2.61) (original
506 magnification 630) (Leica Microsystems, Wetzlar, Germany).

507

508 **Study design of the *in vivo* experiments**

509 In a first cohort, AAVs-CRISPR/SaCas9 were stereotactically delivered into the right SNc of wild-
510 type rats. Afterward, *in vivo* PET scans with imaging markers of VMAT2 expression, dopamine
511 availability, nerve terminal integrity, and inflammatory responses were performed in VMAT2
512 knockdown and control rats using [^{11}C]DTBZ, [^{11}C]raclopride, [^{11}C]methylphenidate, and [^{18}F]GE-
513 180, respectively. Motor consequences of the CRISPR/SaCas9-induced VMAT2 knockdown
514 were explored in a wide spectrum of behavioral tasks. Finally, biochemical and histological
515 analyses were performed to corroborate the *in vivo* data (Fig. 2,3,4a).
516 In a second cohort, cylinder test and [^{11}C]raclopride-PET/BOLD-fMRI scans were performed at
517 baseline and after CRISPR/SaCas9-induced VMAT2 knockdown. These measurements were
518 paralleled by *in vivo* PET scans with imaging markers of VMAT2 and GABA-A expression, to

519 inspect the extent of the induced VMAT2 knockdown and its impact on GABA signaling, using
520 [^{11}C]DTBZ and [^{11}C]flumazenil, respectively (Fig. 5a).
521
522 **Stereotactic injections**

523 Rats were anesthetized by injecting a mixture (1 mL/kg) of fentanyl (0.005 mg/kg), midazolam
524 (2 mg/kg,) and medetomidine (0.15 mg/kg) intraperitoneally, and were placed onto a stereotactic
525 frame (Harvard Apparatus, Holliston, MA, USA) with the skull flat between Lambda and Bregma.
526 The following coordinates were used for the injections (flat skull position): AP: - 5 mm, ML:
527 ± 2 mm, DV: - 7.2 mm, below the dural surface as calculated relative to Bregma. Rats were
528 injected with 3 µL AAVs into the right SNc and were divided into two groups. Control rats (n= 10)
529 were injected with AAV-PHP.EB-sgRNA-*lacZ* (1.7 × 10^{12} gc/mL) and AVV-PHP.EB-SaCas9
530 (1.4 × 10^{12} gc/mL) (1:1 ratio). VMAT2 knockdown rats (n= 47) were injected with AAV-PHP.EB-
531 sgRNA-*Slc18a2* (2.1 × 10^{12} gc/mL) and AVV-PHP.EB-SaCas9 (1.4 × 10^{12} gc/mL) (1:1 ratio) (see
532 Fig. 1a for vector constructs). DPBS (3 µL) was sham-injected into the contralateral SNc.
533 Solutions were infused at a rate of 0.2 µL/min using a 5 µL Hamilton syringe (Hamilton, Bonaduz,
534 Switzerland) and an automated microsyringe pump (Harvard Apparatus, Holliston, MA, USA). To
535 allow for the diffusion of AAVs into the tissue, the needle was left in place for 10 min, and then
536 slowly retracted at 0.2 mm/min. After the surgery, an antidote containing atipamezole
537 (0.75 mg/kg) and flumazenil (0.2 mg/kg) was injected subcutaneously. The rats were kept warm
538 in their cages until fully recovered.
539
540 **Radiotracer synthesis**

541 [^{11}C]CO_2 was produced on a medical cyclotron (PETtrace 860, GE Healthcare, Uppsala, Sweden)
542 using the ^{14}N(p,α)^{11}C route and converted to either [^{11}C]MeI (methyl iodide) or [^{11}C]MeOTf (methyl

543 triflate) using a Tracerlab FX MeI module (GE Healthcare). A Tracerlab FX M module (GE
544 Healthcare) was used for automated methylation, purification, and formulation of the tracers.

545 [^{11}C]Dihydrotetrabenazine (DTBZ), a VMAT2 ligand, was synthesized starting from [^{11}C]MeI,
546 which was reacted with 1 mg (+)-9-O-desmethyl-dihydrotetrabenazine (ABX, Radeberg,
547 Germany) in 300 µl DMF in the presence of 7.5 µl 5 M NaOH for 3 min at 40 °C [108]. Afterward,
548 it was purified by HPLC and formulated as a sterile pyrogen-free saline solution. The total
549 synthesis time from the end of the beam was 45 min. The radiochemical purity of the final
550 radiotracer was > 95% as determined by HPLC. Molar activity at the time of injection was 96 ± 37
551 GBq/µmol.

552 D-threo-[^{11}C]methylphenidate, a dopamine transporter ligand, was synthesized by alkylation of D-
553 threo-N-NPS-ritalinic acid (ABX) using [^{11}C]MeI [109]. After acidic deprotection, purification, and
554 formulation, the product was obtained with a 37 ± 6% decay-corrected radiochemical yield (from
555 [^{11}C]MeI). The total synthesis time was 55 min, and the radiochemical purity of the final
556 formulated radiotracer was > 95% as determined by HPLC analysis. The molar activity was
557 determined at the time of injection as 58 ± 14 GBq/µmol.

558 [^{11}C]Raclopride a D2R ligand, was synthesized by alkylation of S-(+)-O-desmethyl-raclopride
559 (ABX) using [^{11}C]MeOTf. After purification and formulation, the product was obtained with a
560 12 ± 4% decay-corrected radiochemical yield (from [^{11}C]methyl triflate). The total synthesis time
561 from the end of the beam was 55 min. The radiochemical purity of the final formulated radiotracer
562 was > 95% as determined by HPLC. The molar activity was determined at the time of injection
563 and was calculated as 88 ± 41 GBq/µmol.

564 [^{11}C]Flumazenil, a GABA-A ligand, was synthesized by methylation of desmethylflumazenil (ABX)
565 with [^{11}C]MeI. 2 mg of the precursor were dissolved in 0.3 ml DMF with 3 µl 5 M NaOH and
566 reacted for 2 min at 80 °C. After the reaction, the product was purified by semi-preparative HPLC

567 and reformulated by solid-phase extraction (Strata-X, Phenomenex; elution with 0.5 ml ethanol,
568 dilution with 5 ml phosphate-buffered saline). The total synthesis time from the end of the beam
569 was 50 min. The radiochemical purity of the final formulated radiotracer was > 95% as
570 determined by HPLC. The molar activity was determined at the time of injection as
571 109.5 ± 39.6 GBq/µmol.

572 [^{18}F]Fluoride was produced on a PETtrace 860 medical cyclotron (GE Healthcare) using the
573 ^{18}O(p,n)^{18}F route.
574 [^{18}F]GE-180, a translocator protein ligand [110], was synthesized on a FASTlab synthesizer (GE
575 Healthcare) with precursor and reagent kits in single-use cassettes (GE Healthcare) according to
576 the manufacturer's instructions. The radiochemical purity of the final formulated radiotracer was
577 > 95% as determined by HPLC. The molar activity was determined at the time of injection as
578 576 ± 283 GBq/µmol.
579

580 ***In vivo* PET imaging and data analysis**

581 For the study of cohort 1, VMAT2 knockdown (n= 14) and control rats (n= 10) underwent 60 min
582 dynamic PET emission scans with [^{11}C]DTBZ (8 – 10 weeks post-injection), [^{11}C]methylphenidate
583 (10 – 12 weeks post-injection), [^{11}C]raclopride (12 – 14 weeks post-injection) and [^{18}F]GE-180
584 (14 – 16 weeks post-injection) (Fig. 2a). Four rats were excluded from the data analyses because
585 two rats from each group died during a PET acquisition. One control rat was excluded from the
586 [^{11}C]methylphenidate analysis due to a poor signal-to-noise ratio.
587 For the study of cohort 2, VMAT2 knockdown rats (n= 33), underwent 60 min dynamic PET
588 emission acquisitions with [^{11}C]DTBZ (8 – 10 weeks post-injection), and [^{11}C]flumazenil
589 (10 – 12 weeks post-injection). The final cohort included 23 rats (see paragraph Simultaneous
590 PET/fMRI experiments).

591 Three small-animal PET scanners (Inveon, Siemens, Erlangen, Germany) and dedicated rat
592 brain beds (Jomatik Gmbh, Tuebingen, Germany) with stereotactic holders and temperature
593 feedback control units (Medres, Cologne, Germany) were used. These ensured the delivery and
594 removal of the anesthesia gas and stabilized the body temperature at 37 °C during the PET data
595 acquisition. Anesthesia was induced by placing the animals in knock-out boxes and delivering 2%
596 isoflurane in oxygen air. Subsequently, a 24 G catheter (BD Insyte, NJ, USA) was placed into the
597 tail vein for the tracer and/or *i.v.* anesthesia administration. Afterward, animals of cohort 1 were
598 anesthetized with 2% isoflurane vaporized in 1.0 L/min of oxygen. Animals of cohort 2 received a
599 medetomidine bolus injection (0.05 mg/kg) and the anesthesia was switched to constant
600 medetomidine infusion (0.1 mg/kg/h), and 0.5% isoflurane in air during the scan time, as adapted
601 from the literature [111].
602 The rats were placed in the center of the field of view and PET acquisitions started 5 s before the
603 bolus injection of the tracer. In Supplementary Tables 9 and 10, injected activity (MBq/kg) and
604 molar activity (GBq/µmol) at the time of injection are reported for each radioligand. The list-mode
605 data from the dynamic acquisitions of [^{11}C]DTBZ, [^{11}C]raclopride, [^{11}C]methylphenidate, and
606 [^{11}C]flumazenil were histogrammed into 39 time-frames (12x5 s, 6x10 s, 6x30 s, 5x60 s,
607 10x300 s), from [^{18}F]GE-180 into 16 time-frames (5x60 s, 5x120 s, 3x300 s, 3x600 s). PET scans
608 of the study cohort 1 were reconstructed using the OSEM3D map algorithm, and a matrix size of
609 256 x 256 x 159, resulting in a pixel size of 0.38 x 0.38 x 0.79 mm. PET scans of the study cohort
610 2 were reconstructed using the OSEM2D algorithm, and a matrix size of 256 x 256 x 89, resulting
611 in a pixel size of 0.33 x 0.33 x 0.79 mm.
612 Data preprocessing analysis was performed with Matlab (Mathworks, Natick, MA, USA),
613 Statistical Parametric Mapping 12 (SPM12, Wellcome Trust Centre for Neuroimaging, University
614 College London, England), and the QModeling toolbox [112]. First, realignment of all frames was
615 performed using SPM12 and average images were generated for every scan. The mean images
616 were then used for coregistration to the Schiffer rat brain atlas provided by PMOD software [113].

To generate the respective time activity curves (TAC), volumes of interest (VOIs) were defined over the target and reference regions. VOIs were placed over the right and left striatum for [^{11}C]DTBZ, [^{11}C]raclopride, and [^{11}C]methylphenidate, and over the regions reported in Table 2 for [^{11}C]flumazenil. Cerebellum was used as reference region for [^{11}C]DTBZ, [^{11}C]raclopride and [^{11}C]methylphenidate. Pons was used as reference region for [^{11}C]flumazenil.

Binding potentials for [^{11}C]DTBZ, [^{11}C]raclopride, [^{11}C]methylphenidate and [^{11}C]flumazenil were calculated over the all frames in the regions of interest with Logan reference [114], with a population average k2' ([^{11}C]DTBZ: 0.41 min^{-1}, [^{11}C]raclopride: 0.34 min^{-1}, [^{11}C]methylphenidate: 0.18 min^{-1}, [^{11}C]flumazenil: 0.27 min^{-1}). [^{11}C]DTBZ and [^{11}C]raclopride binding changes (%), here expressed as Δ binding, were calculated according to the formula:

$$\Delta\, binding = \frac{1 - \ binding\ right\ striatum}{binding\ left\ striatum} \times 100$$

[^{18}F]GE-180 uptake in the right striatum was calculated over the interval between 30 – 60 min after scan start and normalized by the uptake calculated in the left (DPBS-injected) striatum over the same time interval.

QModeling was used to generate voxel-wise binding potential maps for [^{11}C]DTBZ, [^{11}C]raclopride, [^{11}C]methylphenidate, and [^{11}C]flumazenil. [^{18}F]GE-180 average uptake images were generated with an in-house-written script in MATLAB.

Simultaneous PET/fMRI experiments

Rats (n= 33) underwent longitudinal simultaneous [^{11}C]raclopride-PET/BOLD-fMRI scans at baseline and 8 – 14 weeks after CRISPR/SaCas9-induced VMAT2 knockdown. Three rats had to be excluded from the data analyses due to aliasing artifacts, local distortion, and motion during the data acquisition. Seven rats died during a PET/BOLD-fMRI scan. The final cohort included 23

640 rats. Anesthesia induction and injection were performed as described above for the cohort 2 (see
641 paragraph *In vivo* PET imaging and data analysis).
642 Next, rats were placed onto a dedicated rat bed (Medres, Cologne, Germany) and a temperature
643 feedback control unit (Medres, Cologne, Germany), ensuring the delivery and removal of the
644 anesthesia gas and stabilizing the body temperature at 37 °C during the scan time. A breathing
645 pad and a pulse oximeter were used to observe respiration and heart rates. Scans were acquired
646 using a small-animal 7 T Clinscan MRI scanner, a 72 cm diameter linearly polarized RF coil
647 (Bruker) for transmission, and a four-channel rat brain coil for reception (Bruker Biospin MRI,
648 Ettlingen, Germany). Localizer scans were first acquired to accurately position the rat brains into
649 the center of the PET/MRI field of view. Subsequently, local field homogeneity was optimized by
650 measuring local magnetic field maps. Anatomical reference scans were performed using T2-
651 weighted Turbo-RARE MRI sequences (TR: 1800 ms, TE: 67.11 ms, FOV: 40 x 32 x 32 mm,
652 image size: 160 x 128 x 128 px, Rare factor: 28, averages: 1). Finally, T2*-weighted gradient
653 echo EPI sequences (TR: 2500 ms, TE: 18 ms, 0.25 mm isotropic resolution, FoV 25 x 23 mm,
654 image size: 92 x 85 x 20 px, slice thickness 0.8 mm, slice separation 0.2 mm, 20 slices) were
655 acquired for BOLD-fMRI.
656 A dedicated small-animal PET insert developed in cooperation with Bruker (Bruker Biospin MRI,
657 Ettlingen, Germany) was used for the [^{11}C]raclopride acquisitions, the second generation of a
658 PET insert developed in-house with similar technical specifications [115]. [^{11}C]Raclopride was
659 applied via a bolus injection. In Supplementary Table 10 injected activities (MBq/kg) and molar
660 activities (GBq/µmol) at the time of injection are reported. PET/fMRI acquisitions started
661 simultaneously with the tracer injection and were performed over a period of 60 min. The list-
662 mode files of the PET data were histogrammed into 14 time-frames (1x30 s, 5x60 s, 5x300 s,
663 3x600 s), the 30s between acquisition start and the injection were excluded from the analysis.
664 Reconstruction was performed with an in-house-written OSEM2D algorithm. Data preprocessing
665 and analysis were performed as described above (see paragraph *In vivo* PET imaging and data

666 analysis). A population average k2' ([^{11}C]raclopride baseline: 0.20 min^{-1}, [^{11}C]raclopride VMAT2
667 knockdown: 0.23 min^{-1}) was set for the Logan reference [114].
668 Preprocessing of the fMRI data was performed using a pipeline employing SPM12, Analysis of
669 Functional NeuroImages (AFNI, National Institute of Mental Health (NIMH), Bethesda, Maryland,
670 USA), and in-house-written scripts in MATLAB, as reported previously [116].
671 RS-FC was calculated using a seed-based approach. To this extent, 20 regions were selected
672 from the Schiffer rat brain atlas (a list of the regions is provided in Table 2). The SPM toolbox
673 Marseille Boîte À Région d'Intérêt (MarsBaR) was employed to extract fMRI time-courses from all
674 regions [117]. These were then used to calculate pairwise Pearson's r correlation coefficients for
675 each dataset, generating correlation matrices containing 20 x 20 elements. Self-correlations were
676 set to zero. The computed Pearson's r coefficients then underwent Fischer's transformation into z
677 values for group-level analysis.
678 Several rs-FC metrics were computed on different regional levels to investigate the potential
679 effects of dopamine depletion in the right striatum. Regional node strengths were computed as
680 the sum of all correlations of one seed to the regions included in one network. Interregional node
681 strengths were defined as the sum of the correlations of one node to the regions of another
682 network. Network strengths were defined as the sum of strengths of all correlations between
683 regions belonging to a network. Internetwork strengths were calculated as the sum of all
684 correlations between two sets of regions belonging to two networks [118].
685
686 **Behavioral analysis**
687 *Cylinder test*

688 Untrained rats were placed individually inside a glass cylinder (19 cm Ø, 20 cm height). The test
689 started immediately and lasted 5 min. During the test session rats were left undisturbed and were
690 videotaped with a camera located at the bottom-center of the cylinder to allow a 360 ° angle view.
691 Paw touches were analyzed using a slow-motion video player (VLC software, VideoLan). The

692 number of wall touches, contacts with fully extended digits, was counted. Data were analyzed as
693 follows:

694 $$contralateral\ paw\ touches\ (\%\ to\ total) = \frac{contralateral\ touches}{total\ touches} \times 100$$

695 One rat from the cohort 2 was excluded from the analysis due to issues during video recording.
696

697 *Rotameter test*

698 Rotational asymmetry was assessed using an automated rotameter system composed of four
699 hemispheres (TSE Systems GmBH, Bad Homburg, Germany) based on the design of Ungerstedt
700 and Arbuthnott [119]. Rats were placed into an opaque half bowl (49 cm Ø; 44 cm height) and
701 fixed to a moveable wire with a collar. The number of clockwise (CW) and counterclockwise
702 (CCW) rotations (difference of 42.3° in their position) were automatically counted. The
703 spontaneous rotation test lasted 5 min. Apomorphine-evoked rotational asymmetry was
704 evaluated for 60 min after *s.c.* administration of apomorphine hydrochloride (0.25 mg/kg)
705 dissolved in physiological saline containing 0.1% ascorbic acid (Sigma Aldrich, St. Louis,
706 Missouri, USA). Two priming injections of apomorphine (1-week interval off-drug) were necessary
707 to produce sensitization to the treatment. The program RotaMeter (TSE Systems GmBH, Bad
708 Homburg, Germany) was used to acquire the data. Data were analyzed as follows:

709 $$turns/min = ccw\ rotation\ -\ cw\ rotations$$

710

711 *Beam walk test*

712 Rats were trained for 4 days to cross a built-in-house beam (1.7 cm width, 60 cm length, 40 cm
713 height), and reach a cage with environmental enrichment. Rats had 5 trials to cross the beam
714 with the reward resting time decreasing from 30 s to 10 s. On the test day (one week apart from
715 the fourth day of training), rats were videotaped. The acquired videos were analyzed using a

716 slow-motion video player (VLC software, VideoLan) and the number of footslips (falls) was
717 counted. Data were analyzed as follows:

718 $$contralateral\ footslips\ (\%\ to\ total\ steps) = \frac{contralateral\ footslips}{total\ steps} \times 100$$

719

720 *Open Field test*

721 Untrained rats were set in a rectangular box (TSE Systems GmBH, Bad Homburg, Germany) for
722 11 min (1 min habituation, 10 min test) to evaluate the spontaneous exploratory behavior. A
723 frame with light sensors, as high as the animals' body center, was connected to a receiver box to
724 record the rats' walked distance. The program ActiMod (TSE Systems GmBH, Bad Homburg,
725 Germany) was used for the analysis and the experimental session was divided into 1 min time
726 bins. Results were averaged from the total traveled distance over 10 min (mean ± SD).

727

728 *Body weight gain*

729 Rats' body weight was measured before (week 0) and 14 weeks after CRISPR/SaCas9-induced
730 VMAT2 knockdown. Body weight gain was calculated as follows:

731 $$body\ weight\ gain\ (g) = \frac{weight\ at\ week\ 14 - weight\ at\ week\ 0}{weight\ at\ week\ 0} \times 100$$

732

733 **Histology of rat brain slices**

734 Rats of cohort 1 (n= 20) were sacrificed 19 weeks after viral vector injection via CO_2 inhalation
735 followed by intracardial perfusion with heparinized DPBS (1:50 v/v, 100 mL). After decapitation,
736 brains were rapidly removed and placed in a brain matrix on ice. The left and right striata were
737 dissected, from 2 mm thick coronal sections, flash-frozen in liquid nitrogen, and stored at – 80 °C
738 until further analysis (HPLC). The remaining tissue was fixed in 4% paraformaldehyde for 48 h

739 and then transferred to a 20% sucrose solution for cryoprotection. Brains were cut into 35 µm
740 thick coronal sections on a freezing microtome (Leica Biosystems, Wetzlar, Germany) and stored
741 in an anti-freeze solution (0.5 M phosphate buffer, 30 % glycerol, 30 % ethylene glycol) at
742 - 20 °C. Sections were collected in 12 equally spaced series through the entire anterior-posterior
743 extent of the SN and striatum and stored until further analysis. Immunohistochemistry was
744 performed on free-floating sections. Sections were washed 3 times with TBS buffer and antigen
745 retrieval was carried for 30 min at 80 °C in Tris/EDTA buffer. Afterward, pre-incubation in MeOH
746 (10%) and H_2O_2 (3%) in TBS was performed for 30 min. Following the blocking in 5% normal goat
747 serum in TBS-X (0.05%), primary antibody incubation was performed for 24 h at room
748 temperature in 1% BSA in TBS-X (TH: 1:5000, P40101, Pel-freez, Arkansas, USA, VMAT2:
749 1:5000, 20042, Immunostar, Hudson, USA). The tissue was rinsed in TBS-X and reacted with the
750 respective biotinylated secondary antibody (1:200, Vector Laboratories Ltd., Peterborough, UK)
751 for 60 min at room temperature in 1% BSA in TBS-X. Staining was developed using 3,3'-
752 diaminobenzidine (DAB Substrate Kit, Vector Laboratories Ltd., Peterborough, UK) and an
753 immunoperoxidase system (Vectastain Elite ABC-Kit, Vector Laboratories Ltd., Peterborough,
754 UK). Slices were rinsed, mounted onto chromalum gelatinized slides, dehydrated in ascending
755 concentrations of alcohol and xylene baths, and coverslipped with DPX mounting medium (Sigma
756 Aldrich, St. Louis, Missouri, USA).
757

758 **Stereological analysis**

759 Estimates of total numbers of TH+ cells in nigral sections were obtained with an unbiased
760 stereological quantification method by employing the optical fractionator principle [120]. Brain
761 sections from 5 rats (VMAT2 knockdown n= 2, Control n= 3) were excluded from the stereological
762 analysis, due to weak TH immunoreactivity. First, 5x images were acquired with the automated
763 Metafer slide scanning platform (MetaSystems, Altlußheim, Germany). Then, ROIs were drawn
764 using the VSViewer program (Metasystems, Altlußheim, Germany), and a sampling fraction of

765 50% was defined. Afterward, 63x images were acquired in an automated fashion based on the
766 sampling fraction in a random orientation within the ROI. The acquired 63x images were imported
767 into the VIS program and cell counting was performed with the CAST module (Visiopharm A/S,
768 Hørsholm, Denmark, Version 2020.08.2.8800).
769 The number of cells estimates was obtained by applying the formula:

770 $$Total\ number\ of\ TH+\ cells = \sum\left(\frac{Number\ of\ cells\ counted\ per\ brain}{Acquisition\ fraction\ x\ counting\ frame}\right) \times number\ of\ series$$

771

772 **Immunofluorescence of rat brain slices**

773 Immunofluorescence was performed on SN sections from rats of cohort 1 (35 µm thick coronal
774 sections), mounted onto chromalum gelatinized slides, dehydrated in ascending concentrations of
775 alcohol and xylene baths. Sections were washed 3 times with KPBS buffer and antigen retrieval
776 was carried for 30 min at 80 °C in Tris/EDTA buffer. Following blocking in 5% donkey serum and
777 normal horse serum in KPBS-X (0.25%), primary antibody incubation was performed for 24 h at
778 room temperature (VMAT2: 1:5000, 20042, Immunostar, Hudson, USA, HA-tag: 1:5000, MMS-
779 101R, Nordic BioSite, Taby, Sweden, GFP: 1:50.000, ab13970, Abcam, Cambridge, UK). The
780 tissue was rinsed in KPBS-X and reacted with the respective fluorophore-conjugated secondary
781 antibody (1:200, Vector Laboratories Ltd., Peterborough, UK) for 2 h in 0.2% KPBS-X. Slides
782 were coverslipped with Vectashield mounting medium (Vector Laboratories Ltd., Peterborough,
783 UK).

784

785 **Biochemistry**

786 Dopamine, 3,4-Dihydroxyphenylacetic acid (DOPAC), homovanillic acid (HVA), and serotonin (5-
787 HT) striatal levels were determined by HPLC. Brain samples from 5 rats (VMAT2 knockdown

788 n= 3, Control n= 2) were excluded from the analysis as striatal sections did not fall in the selected
789 range: 1.2 – 0.4 mm.
790 Briefly, striatal brain lysates generated from cohort 1 were injected by a cooled autosampler into
791 an ESA Coulchem III coupled to a Decade Elite electrochemical detector (Antec Scientific,
792 Zoeterwoude, The Netherlands) set to a potential of +350 mV. Separation was facilitated by using
793 an Atlantis Premier BEH C18 AX column (Waters Corporation, Massachusetts, USA) and a dual
794 mobile phase gradient of decreasing octane sulfonic acid (OSA) and increasing MeOH content
795 (mobile phase A containing 100 mM PO_4-buffer pH 2.50 and 4.62 mM OSA and mobile phase B
796 containing 100 mM PO_4-buffer pH 2.50 and 2.31 mM OSA), delivered at a flow rate of
797 0.35 mL/min to an Atlantis Premier BEH C18 column (particle size 2.5 µm, 2.1 mm x 150 mm)
798 (Waters Corporation, Massachusetts, USA). Data was collected using the Chemstation software
799 (Agilent, California, USA) and then exported to Chromeleon (LifeTechnologies, Massachusetts,
800 USA) for data quality control, peak integration, and concentration calculations. Striatal
801 metabolites' content was expressed in nmol for each sample and normalized to total protein (mg).
802 Dopamine turnover rate was calculated according to the formula:

804 $$Dopamine\ turnover\ rate = \frac{HVA + DOPAC}{DA}$$

803

805 **Statistics**

806 Statistical analysis was performed with GraphPad Prism 9.0 (Graphpad Software) if not otherwise
807 stated. Results were analyzed using paired t-tests for the within-subjects comparisons, and
808 unpaired t-tests for the between-groups comparisons. Correlations were performed using linear
809 regression analyses. Synaptic dysfunction discrimination was tested with multiple-comparison
810 ANOVA.

811

Bibliography

1. Biswal, B., et al., *Functional connectivity in the motor cortex of resting human brain using echo-planar MRI.* Magn Reson Med, 1995. **34**(4): p. 537-41.
2. Ogawa, S., et al., *Brain magnetic resonance imaging with contrast dependent on blood oxygenation.* Proc Natl Acad Sci U S A, 1990. **87**(24): p. 9868-72.
3. Lu, H., et al., *Rat brains also have a default mode network.* Proc Natl Acad Sci U S A, 2012. **109**(10): p. 3979-84.
4. Becerra, L., et al., *Robust reproducible resting state networks in the awake rodent brain.* PLoS One, 2011. **6**(10): p. e25701.
5. Fox, M.D., et al., *The human brain is intrinsically organized into dynamic, anticorrelated functional networks.* Proc Natl Acad Sci U S A, 2005. **102**(27): p. 9673-8.
6. Jonckers, E., et al., *Functional connectivity fMRI of the rodent brain: comparison of functional connectivity networks in rat and mouse.* PLoS One, 2011. **6**(4): p. e18876.
7. Wehrl, H.F., et al., *Simultaneous PET-MRI reveals brain function in activated and resting state on metabolic, hemodynamic and multiple temporal scales.* Nat Med, 2013. **19**(9): p. 1184-9.
8. Amend, M., et al., *Functional resting-state brain connectivity is accompanied by dynamic correlations of application-dependent [(18)F]FDG PET-tracer fluctuations.* Neuroimage, 2019. **196**: p. 161-172.
9. Ionescu, T.M., et al., *Elucidating the complementarity of resting-state networks derived from dynamic [(18)F]FDG and hemodynamic fluctuations using simultaneous small-animal PET/MRI.* Neuroimage, 2021. **236**: p. 118045.
10. Badhwar, A., et al., *Resting-state network dysfunction in Alzheimer's disease: A systematic review and meta-analysis.* Alzheimers Dement (Amst), 2017. **8**: p. 73-85.
11. Bluhm, R.L., et al., *Spontaneous low-frequency fluctuations in the BOLD signal in schizophrenic patients: anomalies in the default network.* Schizophr Bull, 2007. **33**(4): p. 1004-12.
12. Volkow, N.D., et al., *Imaging endogenous dopamine competition with [11C]raclopride in the human brain.* Synapse, 1994. **16**(4): p. 255-62.
13. Laruelle, M., *Imaging synaptic neurotransmission with in vivo binding competition techniques: a critical review.* J Cereb Blood Flow Metab, 2000. **20**(3): p. 423-51.
14. Patel, V.D., et al., *Imaging dopamine release with Positron Emission Tomography (PET) and (11)C-raclopride in freely moving animals.* Neuroimage, 2008. **41**(3): p. 1051-66.
15. Roffman, J.L., et al., *Dopamine D1 signaling organizes network dynamics underlying working memory.* Science advances, 2016. **2**(6): p. e1501672-e1501672.
16. McCutcheon, R.A., et al., *Mesolimbic Dopamine Function Is Related to Salience Network Connectivity: An Integrative Positron Emission Tomography and Magnetic Resonance Study.* Biol Psychiatry, 2019. **85**(5): p. 368-378.
17. Nagano-Saito, A., et al., *Posterior dopamine D2/3 receptors and brain network functional connectivity.* Synapse, 2017. **71**(11).
18. Hahn, A., et al., *Differential modulation of the default mode network via serotonin-1A receptors.* Proc Natl Acad Sci U S A, 2012. **109**(7): p. 2619-24.
19. Vidal, B., et al., *In vivo biased agonism at 5-HT(1A) receptors: characterisation by simultaneous PET/MR imaging.* Neuropsychopharmacology, 2018. **43**(11): p. 2310-2319.
20. Shiyam Sundar, L.K., et al., *Fully Integrated PET/MR Imaging for the Assessment of the Relationship Between Functional Connectivity and Glucose Metabolic Rate.* Front Neurosci, 2020. **14**: p. 252.
21. Sander, C.Y., et al., *Imaging Agonist-Induced D2/D3 Receptor Desensitization and Internalization In Vivo with PET/fMRI.* Neuropsychopharmacology, 2016. **41**(5): p. 1427-36.

858 22. Ionescu, T.M., et al., *Striatal and prefrontal D2R and SERT distributions contrastingly correlate with*
859 *default-mode connectivity.* Neuroimage, 2021. **243**: p. 118501.
860 23. Betley, J.N. and S.M. Sternson, *Adeno-associated viral vectors for mapping, monitoring, and*
861 *manipulating neural circuits.* Hum Gene Ther, 2011. **22**(6): p. 669-77.
862 24. Jinek, M., et al., *RNA-programmed genome editing in human cells.* Elife, 2013. **2**: p. e00471.
863 25. Cong, L., et al., *Multiplex genome engineering using CRISPR/Cas systems.* Science, 2013. **339**(6121):
864 p. 819-23.
865 26. Whitworth, K.M., et al., *Use of the CRISPR/Cas9 system to produce genetically engineered pigs from*
866 *in vitro-derived oocytes and embryos.* Biol Reprod, 2014. **91**(3): p. 78.
867 27. Chen, Y., et al., *Functional disruption of the dystrophin gene in rhesus monkey using CRISPR/Cas9.*
868 Hum Mol Genet, 2015. **24**(13): p. 3764-74.
869 28. Chang, N., et al., *Genome editing with RNA-guided Cas9 nuclease in zebrafish embryos.* Cell Res,
870 2013. **23**(4): p. 465-72.
871 29. Platt, R.J., et al., *CRISPR-Cas9 knockin mice for genome editing and cancer modeling.* Cell, 2014.
872 **159**(2): p. 440-55.
873 30. Yu, Z., et al., *Highly efficient genome modifications mediated by CRISPR/Cas9 in Drosophila.*
874 Genetics, 2013. **195**(1): p. 289-91.
875 31. Musunuru, K., et al., *In vivo CRISPR base editing of PCSK9 durably lowers cholesterol in primates.*
876 Nature, 2021. **593**(7859): p. 429-434.
877 32. Ousterout, D.G., et al., *Multiplex CRISPR/Cas9-based genome editing for correction of dystrophin*
878 *mutations that cause Duchenne muscular dystrophy.* Nat Commun, 2015. **6**: p. 6244.
879 33. Swiech, L., et al., *In vivo interrogation of gene function in the mammalian brain using CRISPR-Cas9.*
880 Nature Biotechnology, 2015. **33**(1): p. 102-U286.
881 34. Wilbie, D., J. Walther, and E. Mastrobattista, *Delivery Aspects of CRISPR/Cas for in Vivo Genome*
882 *Editing.* Accounts of chemical research, 2019. **52**(6): p. 1555-1564.
883 35. Wu, W.Y., et al., *Genome editing by natural and engineered CRISPR-associated nucleases.* Nat Chem
884 Biol, 2018. **14**(7): p. 642-651.
885 36. Zetsche, B., et al., *Cpf1 is a single RNA-guided endonuclease of a class 2 CRISPR-Cas system.* Cell,
886 2015. **163**(3): p. 759-71.
887 37. Kleinstiver, B.P., et al., *Engineered CRISPR-Cas9 nucleases with altered PAM specificities.* Nature,
888 2015. **523**(7561): p. 481-5.
889 38. Ran, F.A., et al., *In vivo genome editing using Staphylococcus aureus Cas9.* Nature, 2015. **520**(7546):
890 p. 186-91.
891 39. Nishimasu, H., et al., *Crystal Structure of Staphylococcus aureus Cas9.* Cell, 2015. **162**(5): p. 1113-
892 26.
893 40. Sun, H., et al., *Development of a CRISPR-SaCas9 system for projection- and function-specific gene*
894 *editing in the rat brain.* Sci Adv, 2020. **6**(12): p. eaay6687.
895 41. Kumar, N., et al., *The Development of an AAV-Based CRISPR SaCas9 Genome Editing System That*
896 *Can Be Delivered to Neurons in vivo and Regulated via Doxycycline and Cre-Recombinase.* Front Mol
897 Neurosci, 2018. **11**: p. 413.
898 42. Hunker, A.C., et al., *Conditional Single Vector CRISPR/SaCas9 Viruses for Efficient Mutagenesis in*
899 *the Adult Mouse Nervous System.* Cell Rep, 2020. **30**(12): p. 4303-4316 e6.
900 43. Liu, Y. and R.H. Edwards, *The role of vesicular transport proteins in synaptic transmission and neural*
901 *degeneration.* Annu Rev Neurosci, 1997. **20**: p. 125-56.
902 44. Miyanishi, K., et al., *Behavioral tests predicting striatal dopamine level in a rat hemi-Parkinson's*
903 *disease model.* Neurochem Int, 2019. **122**: p. 38-46.
904 45. Tomasi, D., et al., *Dopamine transporters in striatum correlate with deactivation in the default mode*
905 *network during visuospatial attention.* PLoS One, 2009. **4**(6): p. e6102.

46. Sambataro, F., et al., *DRD2 genotype-based variation of default mode network activity and of its relationship with striatal DAT binding.* Schizophr Bull, 2013. **39**(1): p. 206-16.
47. Tritsch, N.X., J.B. Ding, and B.L. Sabatini, *Dopaminergic neurons inhibit striatal output through non-canonical release of GABA.* Nature, 2012. **490**(7419): p. 262-6.
48. Tritsch, N.X., et al., *Midbrain dopamine neurons sustain inhibitory transmission using plasma membrane uptake of GABA, not synthesis.* Elife, 2014. **3**: p. e01936.
49. Chatterjee, D., et al., *Enhanced CNS transduction from AAV.PHP.eB infusion into the cisterna magna of older adult rats compared to AAV9.* Gene Ther, 2021.
50. Hume, S.P., et al., *Effect of L-dopa and 6-hydroxydopamine lesioning on [11C]raclopride binding in rat striatum, quantified using PET.* Synapse, 1995. **21**(1): p. 45-53.
51. Mishra, R.K., A.M. Marshall, and S.L. Varmuza, *Supersensitivity in rat caudate nucleus: effects of 6-hydroxydopamine on the time course of dopamine receptor and cyclic AMP changes.* Brain Res, 1980. **200**(1): p. 47-57.
52. Creese, I., D.R. Burt, and S.H. Snyder, *Dopamine receptor binding enhancement accompanies lesion-induced behavioral supersensitivity.* Science, 1977. **197**(4303): p. 596-8.
53. Konieczny, J., et al., *The significance of rotational behavior and sensitivity of striatal dopamine receptors in hemiparkinsonian rats: A comparative study of lactacystin and 6-OHDA.* Neuroscience, 2017. **340**: p. 308-318.
54. Wang, Y.M., et al., *Knockout of the vesicular monoamine transporter 2 gene results in neonatal death and supersensitivity to cocaine and amphetamine.* Neuron, 1997. **19**(6): p. 1285-96.
55. Seeman, P., et al., *Dopamine receptors in the central nervous system.* Fed Proc, 1978. **37**(2): p. 131-6.
56. Gnanalingham, K.K. and R.G. Robertson, *The effects of chronic continuous versus intermittent levodopa treatments on striatal and extrastriatal D1 and D2 dopamine receptors and dopamine uptake sites in the 6-hydroxydopamine lesioned rat--an autoradiographic study.* Brain Res, 1994. **640**(1-2): p. 185-94.
57. Graham, W.C., A.R. Crossman, and G.N. Woodruff, *Autoradiographic studies in animal models of hemi-parkinsonism reveal dopamine D2 but not D1 receptor supersensitivity. I. 6-OHDA lesions of ascending mesencephalic dopaminergic pathways in the rat.* Brain Res, 1990. **514**(1): p. 93-102.
58. Antonini, A., et al., *Long-term changes of striatal dopamine D2 receptors in patients with Parkinson's disease: a study with positron emission tomography and [11C]raclopride.* Mov Disord, 1997. **12**(1): p. 33-8.
59. Kraemmer, J., et al., *Correlation of striatal dopamine transporter imaging with post mortem substantia nigra cell counts.* Mov Disord, 2014. **29**(14): p. 1767-73.
60. Sossi, V., et al., *Dopamine transporter relation to levodopa-derived synaptic dopamine in a rat model of Parkinson's: an in vivo imaging study.* J Neurochem, 2009. **109**(1): p. 85-92.
61. Zigmond, M.J., T.G. Hastings, and R.G. Perez, *Increased dopamine turnover after partial loss of dopaminergic neurons: compensation or toxicity?* Parkinsonism Relat Disord, 2002. **8**(6): p. 389-93.
62. Takahashi, N., et al., *VMAT2 knockout mice: heterozygotes display reduced amphetamine-conditioned reward, enhanced amphetamine locomotion, and enhanced MPTP toxicity.* Proc Natl Acad Sci U S A, 1997. **94**(18): p. 9938-43.
63. Fon, E.A., et al., *Vesicular transport regulates monoamine storage and release but is not essential for amphetamine action.* Neuron, 1997. **19**(6): p. 1271-83.
64. Mooslehner, K.A., et al., *Mice with very low expression of the vesicular monoamine transporter 2 gene survive into adulthood: potential mouse model for parkinsonism.* Mol Cell Biol, 2001. **21**(16): p. 5321-31.
65. Caudle, W.M., et al., *Reduced vesicular storage of dopamine causes progressive nigrostriatal neurodegeneration.* J Neurosci, 2007. **27**(30): p. 8138-48.

954 66. Taylor, T.N., et al., *Nonmotor symptoms of Parkinson's disease revealed in an animal model with*
955 *reduced monoamine storage capacity.* J Neurosci, 2009. **29**(25): p. 8103-13.
956 67. Back, S., et al., *Neuron-Specific Genome Modification in the Adult Rat Brain Using CRISPR-Cas9*
957 *Transgenic Rats.* Neuron, 2019.
958 68. Zimmer, E.R., et al., *MicroPET imaging and transgenic models: a blueprint for Alzheimer's disease*
959 *clinical research.* Trends Neurosci, 2014. **37**(11): p. 629-41.
960 69. Andrews-Hanna, J.R., *The brain's default network and its adaptive role in internal mentation.*
961 Neuroscientist, 2012. **18**(3): p. 251-70.
962 70. Gottlich, M., et al., *Altered resting state brain networks in Parkinson's disease.* PLoS One, 2013.
963 **8**(10): p. e77336.
964 71. Huang, S., et al., *Multisensory Competition Is Modulated by Sensory Pathway Interactions with*
965 *Fronto-Sensorimotor and Default-Mode Network Regions.* J Neurosci, 2015. **35**(24): p. 9064-77.
966 72. Wu, C.W., et al., *Synchrony Between Default-Mode and Sensorimotor Networks Facilitates Motor*
967 *Function in Stroke Rehabilitation: A Pilot fMRI Study.* Front Neurosci, 2020. **14**: p. 548.
968 73. Wang, J., et al., *Functional reorganization of intra- and internetwork connectivity in major*
969 *depressive disorder after electroconvulsive therapy.* Hum Brain Mapp, 2018. **39**(3): p. 1403-1411.
970 74. Perlbarg, V., et al., *Alterations of the nigrostriatal pathway in a 6-OHDA rat model of Parkinson's*
971 *disease evaluated with multimodal MRI.* PLoS One, 2018. **13**(9): p. e0202597.
972 75. Monnot, C., et al., *Asymmetric dopaminergic degeneration and levodopa alter functional*
973 *corticostriatal connectivity bilaterally in experimental parkinsonism.* Exp Neurol, 2017. **292**: p. 11-
974 20.
975 76. Honey, G.D., et al., *Dopaminergic drug effects on physiological connectivity in a human cortico-*
976 *striato-thalamic system.* Brain, 2003. **126**(Pt 8): p. 1767-81.
977 77. Kwak, Y., et al., *Altered resting state cortico-striatal connectivity in mild to moderate stage*
978 *Parkinson's disease.* Front Syst Neurosci, 2010. **4**: p. 143.
979 78. Costa, R.M., et al., *Rapid alterations in corticostriatal ensemble coordination during acute*
980 *dopamine-dependent motor dysfunction.* Neuron, 2006. **52**(2): p. 359-69.
981 79. Gatev, P., O. Darbin, and T. Wichmann, *Oscillations in the basal ganglia under normal conditions*
982 *and in movement disorders.* Mov Disord, 2006. **21**(10): p. 1566-77.
983 80. Hammond, C., H. Bergman, and P. Brown, *Pathological synchronization in Parkinson's disease:*
984 *networks, models and treatments.* Trends Neurosci, 2007. **30**(7): p. 357-64.
985 81. Eusebio, A., et al., *Resonance in subthalamo-cortical circuits in Parkinson's disease.* Brain, 2009.
986 **132**(Pt 8): p. 2139-50.
987 82. Brazhnik, E., et al., *State-dependent spike and local field synchronization between motor cortex and*
988 *substantia nigra in hemiparkinsonian rats.* J Neurosci, 2012. **32**(23): p. 7869-80.
989 83. Moran, R.J., et al., *Alterations in brain connectivity underlying beta oscillations in Parkinsonism.*
990 PLoS Comput Biol, 2011. **7**(8): p. e1002124.
991 84. Gerfen, C.R. and D.J. Surmeier, *Modulation of striatal projection systems by dopamine.* Annu Rev
992 Neurosci, 2011. **34**: p. 441-66.
993 85. Caspers, J., et al., *Differential Functional Connectivity Alterations of Two Subdivisions within the*
994 *Right dlPFC in Parkinson's Disease.* Front Hum Neurosci, 2017. **11**: p. 288.
995 86. Owens-Walton, C., et al., *Increased functional connectivity of thalamic subdivisions in patients with*
996 *Parkinson's disease.* PLoS One, 2019. **14**(9): p. e0222002.
997 87. Kahn, I., et al., *Distinct cortical anatomy linked to subregions of the medial temporal lobe revealed*
998 *by intrinsic functional connectivity.* J Neurophysiol, 2008. **100**(1): p. 129-39.
999 88. Vincent, J.L., et al., *Coherent spontaneous activity identifies a hippocampal-parietal memory*
1000 *network.* J Neurophysiol, 2006. **96**(6): p. 3517-31.
1001 89. Hillary, F.G., et al., *Hyperconnectivity is a fundamental response to neurological disruption.*
1002 Neuropsychology, 2015. **29**(1): p. 59-75.

1003 90. Klobusiakova, P., et al., *Connectivity Between Brain Networks Dynamically Reflects Cognitive Status*
1004 *of Parkinson's Disease: A Longitudinal Study.* J Alzheimers Dis, 2019. **67**(3): p. 971-984.
1005 91. Mevel, K., et al., *The default mode network in healthy aging and Alzheimer's disease.* Int J
1006 Alzheimers Dis, 2011. **2011**: p. 535816.
1007 92. Gorges, M., et al., *To rise and to fall: functional connectivity in cognitively normal and cognitively*
1008 *impaired patients with Parkinson's disease.* Neurobiol Aging, 2015. **36**(4): p. 1727-1735.
1009 93. Helmich, R.C., et al., *Spatial remapping of cortico-striatal connectivity in Parkinson's disease.* Cereb
1010 Cortex, 2010. **20**(5): p. 1175-86.
1011 94. O'Gorman Tuura, R.L., C.R. Baumann, and H. Baumann-Vogel, *Beyond Dopamine: GABA, Glutamate,*
1012 *and the Axial Symptoms of Parkinson Disease.* Front Neurol, 2018. **9**: p. 806.
1013 95. Whiting, P.J., *The GABAA receptor gene family: new opportunities for drug development.* Curr Opin
1014 Drug Discov Devel, 2003. **6**(5): p. 648-57.
1015 96. Kapogiannis, D., et al., *Posteromedial cortex glutamate and GABA predict intrinsic functional*
1016 *connectivity of the default mode network.* Neuroimage, 2013. **64**: p. 112-9.
1017 97. Douaud, G., et al., *Integration of structural and functional magnetic resonance imaging in*
1018 *amyotrophic lateral sclerosis.* Brain, 2011. **134**(Pt 12): p. 3470-9.
1019 98. Levar, N., et al., *Anterior cingulate GABA and glutamate concentrations are associated with resting-*
1020 *state network connectivity.* Sci Rep, 2019. **9**(1): p. 2116.
1021 99. Lanoue, A.C., G.J. Blatt, and J.J. Soghomonian, *Decreased parvalbumin mRNA expression in*
1022 *dorsolateral prefrontal cortex in Parkinson's disease.* Brain Res, 2013. **1531**: p. 37-47.
1023 100. Lanoue, A.C., et al., *Decreased glutamic acid decarboxylase mRNA expression in prefrontal cortex in*
1024 *Parkinson's disease.* Exp Neurol, 2010. **226**(1): p. 207-17.
1025 101. Ihara, M., et al., *Association of vascular parkinsonism with impaired neuronal integrity in the*
1026 *striatum.* J Neural Transm (Vienna), 2007. **114**(5): p. 577-84.
1027 102. van Nuland, A.J.M., et al., *GABAergic changes in the thalamocortical circuit in Parkinson's disease.*
1028 Hum Brain Mapp, 2020. **41**(4): p. 1017-1029.
1029 103. Allen, P., et al., *Extrinsic and default mode networks in psychiatric conditions: Relationship to*
1030 *excitatory-inhibitory transmitter balance and early trauma.* Neurosci Biobehav Rev, 2019. **99**: p. 90-
1031 100.
1032 104. Liu, Z., et al., *Tissue Specific Expression of Cre in Rat Tyrosine Hydroxylase and Dopamine Active*
1033 *Transporter-Positive Neurons.* PLoS One, 2016. **11**(2): p. e0149379.
1034 105. Anders Björklund, S.B.D., *Dopamine neuron systems in the brain: an update.* Trends in
1035 Neuroscience, 2007. **30**(5): p. 194-202.
1036 106. Ran, F.A., et al., *Genome engineering using the CRISPR-Cas9 system.* Nat Protoc, 2013. **8**(11): p.
1037 2281-2308.
1038 107. Vouillot, L., A. Thelie, and N. Pollet, *Comparison of T7E1 and surveyor mismatch cleavage assays to*
1039 *detect mutations triggered by engineered nucleases.* G3 (Bethesda), 2015. **5**(3): p. 407-15.
1040 108. Huang, Z.R., et al., *A Novel Potential Positron Emission Tomography Imaging Agent for Vesicular*
1041 *Monoamine Transporter Type 2.* PLoS One, 2016. **11**(9): p. e0161295.
1042 109. Ding, Y.S., et al., *Pharmacokinetics and in vivo specificity of [11C]dl-threo-methylphenidate for the*
1043 *presynaptic dopaminergic neuron.* Synapse, 1994. **18**(2): p. 152-60.
1044 110. Wadsworth, H., et al., *[(1)(8)F]GE-180: a novel fluorine-18 labelled PET tracer for imaging*
1045 *Translocator protein 18 kDa (TSPO).* Bioorg Med Chem Lett, 2012. **22**(3): p. 1308-13.
1046 111. Paasonen, J., et al., *Functional connectivity under six anesthesia protocols and the awake condition*
1047 *in rat brain.* Neuroimage, 2018. **172**: p. 9-20.
1048 112. Lopez-Gonzalez, F.J., et al., *QModeling: a Multiplatform, Easy-to-Use and Open-Source Toolbox for*
1049 *PET Kinetic Analysis.* Neuroinformatics, 2019. **17**(1): p. 103-114.
1050 113. Schiffer, W.K., et al., *Serial microPET measures of the metabolic reaction to a microdialysis probe*
1051 *implant.* J Neurosci Methods, 2006. **155**(2): p. 272-84.

114. Logan, J., *Graphical analysis of PET data applied to reversible and irreversible tracers.* Nucl Med Biol, 2000. **27**(7): p. 661-70.
115. Judenhofer, M.S., et al., *Simultaneous PET-MRI: a new approach for functional and morphological imaging.* Nat Med, 2008. **14**(4): p. 459-65.
116. Ionescu, T., *Striatal and prefrontal D2R and SERT distributions contrastingly correlate with default-mode connectivity.* 2021.
117. Matthew Brett, J.-L.A., Romain Valabregue, Jean-Baptiste Poline, *Region of interest analysis using an SPM toolbox*, in *8th Internation Conference on Functional Mapping of the Human Brain*. June 2-6, 2002: Sendai, Japan.
118. Rubinov, M. and O. Sporns, *Complex network measures of brain connectivity: uses and interpretations.* Neuroimage, 2010. **52**(3): p. 1059-69.
119. Ungerstedt, U. and G.W. Arbuthnott, *Quantitative recording of rotational behavior in rats after 6-hydroxy-dopamine lesions of the nigrostriatal dopamine system.* Brain Res, 1970. **24**(3): p. 485-93.
120. West, M.J., *Stereological methods for estimating the total number of neurons and synapses: issues of precision and bias.* Trends Neurosci, 1999. **22**(2): p. 51-61.

Acknowledgments

We are very grateful to Feng Zhang and all members of the laboratory, Broad Institute of MIT and Harvard, for the help and support with establishing the CRISPR gene knockdown experiments. We thank the technical assistants Sandro Aidone, Daniel Bukala, Linda Schramm, Maren Harant, Ramona Stremme, Elena Kimmerle and Johannes Kinzler. We also thank Ulla Samuelsson, Ulrika Sparrhult-Björk, Dr. Ulrika Schagerlöf, Anneli Josefsson and Anna Hansen at Lund University, Sweden for their technical support. Additionally, we acknowledge Dr. Julia Mannheim, Dr. Andreas Schmid, Dr. Rebecca Rock, Ines Herbon, Dr. Neele Hübner, Dr. Andreas Dieterich, Hans Jörg Rahm, Dr. Carsten Calaminus, Funda Cay, Kristin Patzwaldt, Laura Kübler, Marilena Poxleitner, Sabrina Buss and Dominik Seyfried for their administrative, technical, and experimental support at the Department of Preclinical Imaging and Radiopharmacy, Werner Siemens Imaging Center, Eberhard Karls University, Tuebingen. This study is also part of the PhD theses of Sabina Marciano and Tudor Mihai Ionescu.

Funding

- German Research Foundation to KH
- Carl-Zeiss Foundation to KH
- Werner Siemens Foundation to BJP
- Deutscher Akademischer Austauschdienst to SM, KH

Author contributions

- Conceptualization: KH
- Methodology: SM, TMI
- Software: SM, TMI
- Validation: SM
- Formal analysis: SM, TMI

- Investigation: SM, TMI, AM, RSS, RYC
- Resources: BJP, DK
- Data curation: SM
- Writing – original draft: SM
- Writing – review and editing: SM, TMI, AM, DK, RSS, RYC, BJP, KH
- Supervision: KH
- Project administration: KH
- Funding acquisition: BJP, KH

Competing interests

The authors declare no conflict of interest.

Data availability

The original dataset will be made available upon request.

1106 **Figures**

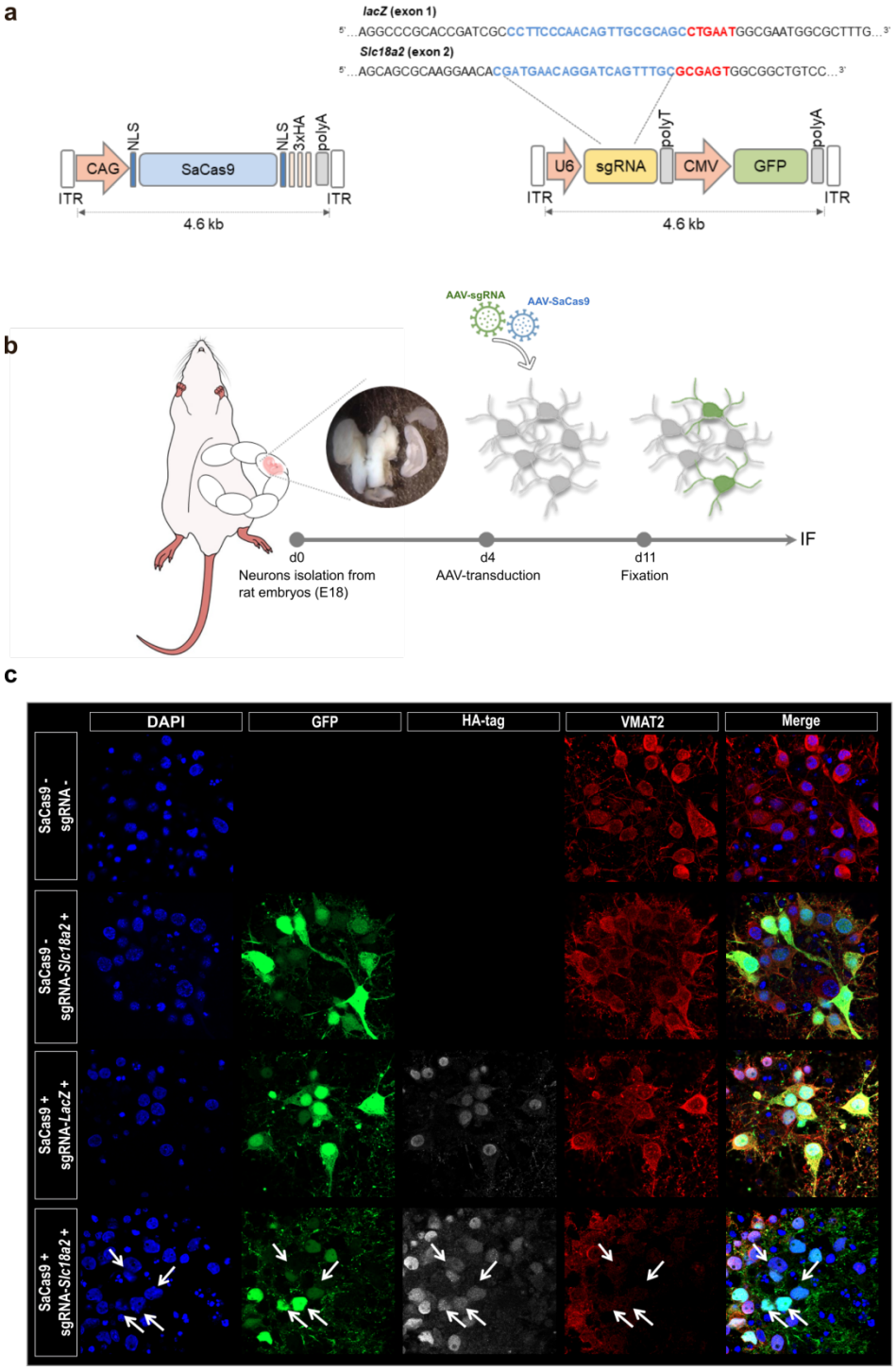

1107

1108 **Fig. 1 *In vitro* validation of CRISPR/SaCas9-induced VMAT2 knockdown in rat primary cortical**
1109 **neurons.** (**a**) AAV-SaCas9 and AAV-sgRNA expression vectors. (**b**) Experimental design for primary
1110 neurons isolation and transduction. (**c**) VMAT2 immunostaining (red), nuclei labeled with DAPI (blue). GFP
1111 (green) and HA-tag (white) indicate the expression of the sgRNA and SaCas9 vectors, respectively. VMAT2
1112 KD (arrows) is shown in neurons transduced with AAVs carrying SaCas9 and sgRNA-*Slc18a2.* KD,

1113 knockdown; ITR, inverted terminal repeat; CMV, cytomegalovirus promoter; GFP, green fluorescent protein;
1114 CAG, CMV enhancer/chicken β-actin promoter; NLS, nuclear localization signal; HA-tag, hemagglutinin tag;
1115 polyA, polyadenylation signal; polyT, polytermination signal.

1116

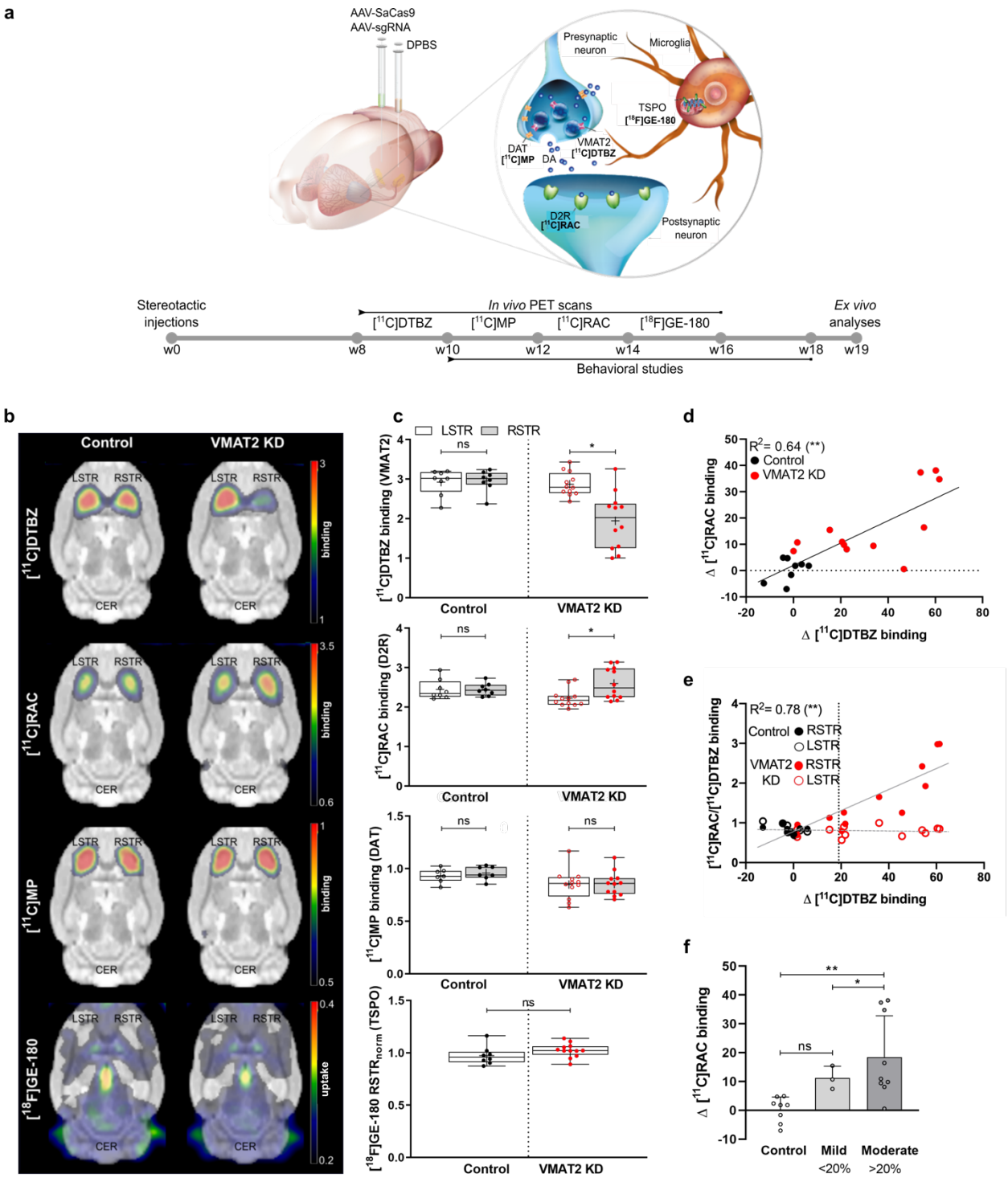

Fig. 2 CRISPR/SaCas9-induced VMAT2 knockdown elicits postsynaptic changes but no nerve terminal loss or neuroinflammation in the adult rat brain. (**a**) Schematic illustration of the experimental design. (**b**) Mean binding potential and uptake maps of control and VMAT2 KD rats co-registered to a rat brain atlas. (**c**) Binding potential values of individual control and VMAT2 KD rats in the left and right striatum. For [^{18}F]GE-180 uptake values normalized to the left striatum are shown. (**d**) A strong correlation between Δ [^{11}C]RAC and Δ [^{11}C]DTBZ binding is shown. (**e**) Ratio of striatal [^{11}C]RAC and [^{11}C]DTBZ binding shows prominent [^{11}C]RAC changes when a threshold of ~ 20% Δ [^{11}C]DTBZ binding is reached. This threshold was

1125 set to separate the VMAT2 KD rats into *mild* and *moderate*. (**f**) *Mild* and *moderate* rats could be differentiated
1126 based on the postsynaptic changes. **P*< 0.01, ***P*< 0.001, Bonferroni-Sidak corrected. Data are shown as
1127 boxplot with the median value (central mark), the mean value (plus sign), interquartile range (boxes edges),
1128 and the extreme points of the distribution (whiskers). Control rats n= 8; VMAT2 KD rats n= 12. *Mild*:
1129 Δ [^{11}C]DTBZ binding < 20%; *Moderate*: Δ [^{11}C]DTBZ binding ≥ 20%. [^{11}C]MP, [^{11}C]methylphenidate;
1130 [^{11}C]RAC, [^{11}C]raclopride; LSTR, left striatum; RSTR, right striatum; CER, cerebellum; KD, knockdown; DAT,
1131 dopamine transporter; TSPO, translocator protein.

1132

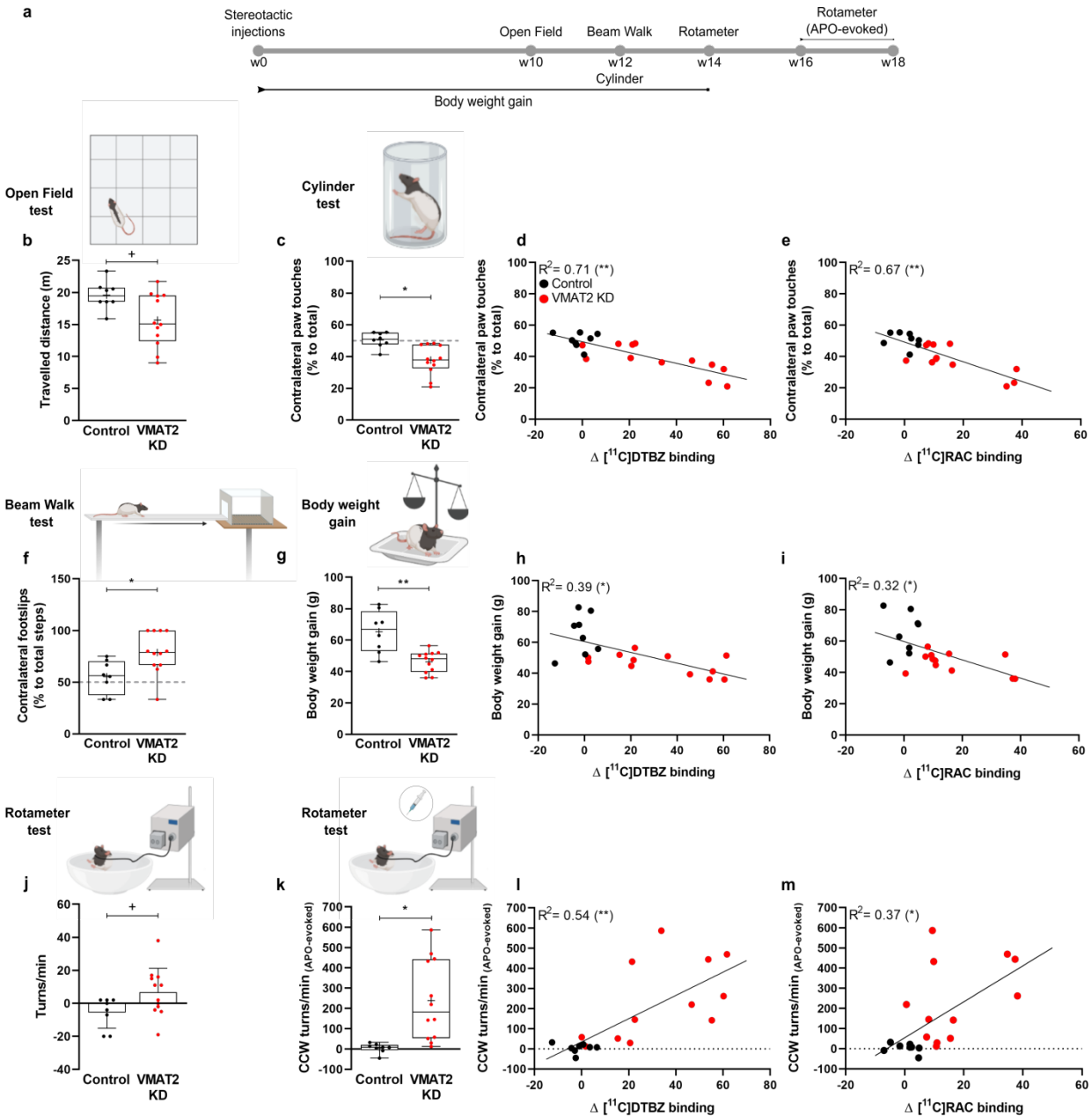

Fig. 3 CRISPR/SaCas9-induced VMAT2 knockdown impairs motor function. (**a**) Schematic illustration of the behavioral tests. (**b**) In the open field test, the distance travelled (m) by VMAT2 KD rats was reduced. (**c**) Cylinder test. VMAT2 KD rats showed a reduction in the contralateral paw touches, compared with controls. Rats performance in the cylinder test strongly correlated with VMAT2 expression changes (Δ [^{11}C]DTBZ binding) and corresponding changes in dopamine availability (Δ [^{11}C]RAC binding) (**d,e**). (**f**) In the beam walk test, VMAT2 KD rats displayed a higher number of footslips to the left contralateral side compared with control rats. (**g**) Body weight assessment 14 weeks after CRISPR/SaCas9 gene-editing showed reduced body weight gain in VMAT2 KD compared with control rats. (**h,i**) Body weight gain correlated with VMAT2 expression changes (Δ [^{11}C]DTBZ binding) and corresponding changes in dopamine availability (Δ [^{11}C]RAC binding). (**j**) Spontaneous rotation in a novel spherical environment showed increased CW rotations in VMAT2 KD rats compared with control rats. (**k**) Apomorphine-evoked rotational behavior. VMAT2 KD rats displayed a higher number of CCW rotations compared with control rats in the rotameter test. (**l,m**) Apomorphine-evoked rotations exhibited a strong correlation with VMAT2 expression changes (Δ [^{11}C]DTBZ

1147 binding) and changes in dopamine availability (Δ [^{11}C]RAC binding). Data are shown as boxplot with the
1148 median value (central mark), the mean value (plus sign), interquartile range (boxes edges), and the extreme
1149 points of the distribution (whiskers). $^{+}P < 0.05$, $^{*}P < 0.01$, $^{**}P < 0.001$. Control rats n= 8; VMAT2 KD rats n= 12.
1150 CCW, counter-clockwise; APO, apomorphine; KD, knockdown; [^{11}C]RAC, [^{11}C]raclopride. Illustrations in the
1151 figure were created with BioRender.com.

1152

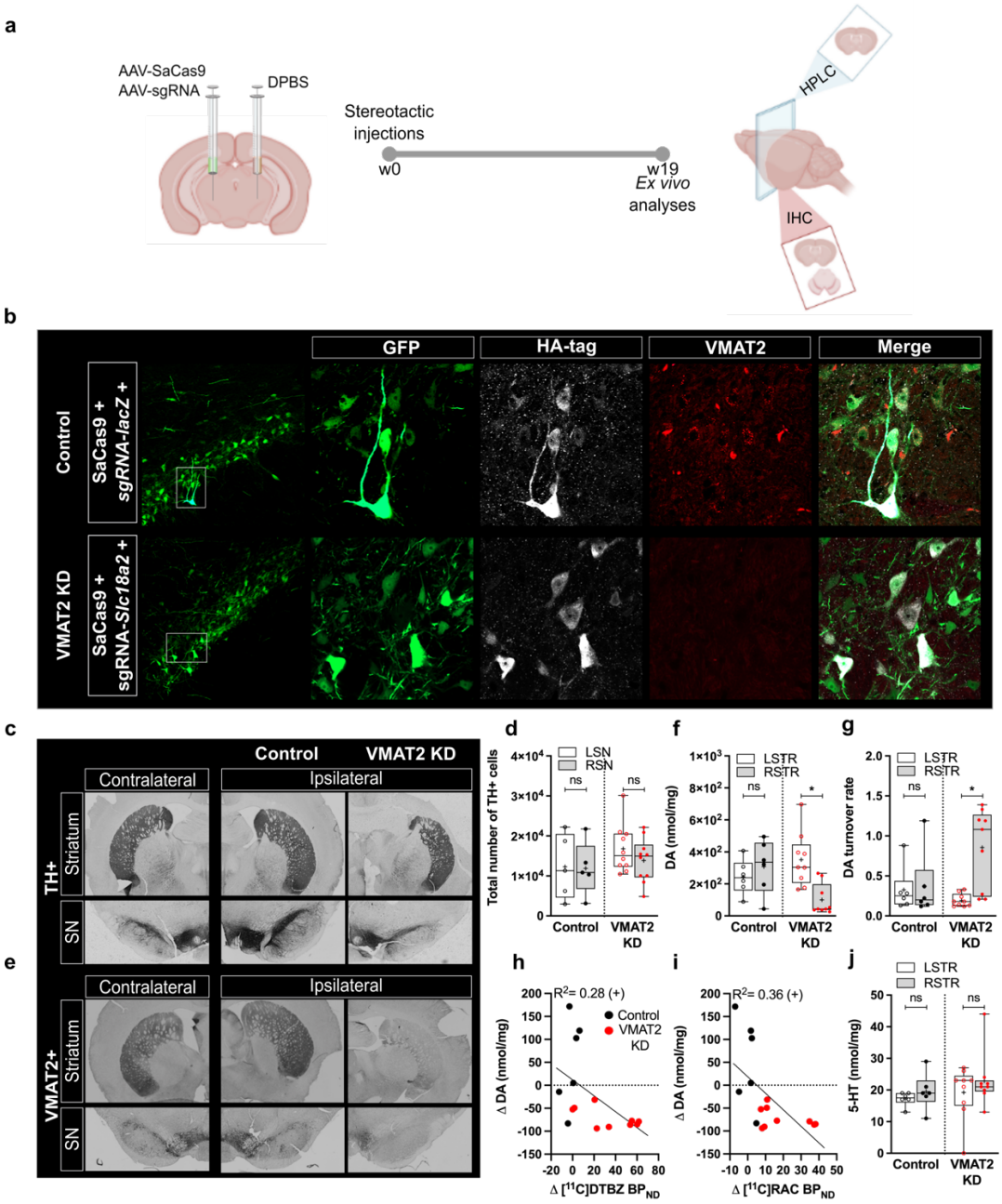

Fig. 4 *Ex vivo* validation of the CRISPR/SaCas9-induced VMAT2 knockdown. (**a**) Schematic illustration of the *ex vivo* analyses. (**b**) Immunofluorescence of nigral sections of control and VMAT2 KD rats confirmed the concomitant expression of SaCas9 and sgRNA. Staining for GFP (AAV-sgRNAs, green), HA-tag (AAV-SaCas9, white), and VMAT2 expression (red) for two exemplary rats is shown. VMAT2 expression was largely reduced in the SNc of VMAT2 KD rats. (**c,d**) TH expression in the ipsilateral and contralateral striatum and SNc of VMAT2 KD (n= 10) and control (n= 5) rats evidenced no cell loss. (**e**) VMAT2 immunohistochemistry in the SNc and striatum confirmed large protein reduction in the ipsilateral hemisphere of VMAT2 KD rats. (**f**) Striatal dopamine, normalized to total protein concentration, was reduced in the ipsilateral striatum of VMAT2 KD (n= 9), but not control (n= 6) rats. This reduction was paralleled by increased metabolic outcome (**g**). (**h,i**) Dopamine changes correlated with the VMAT2 KD extent and postsynaptic changes, deducted from [^{11}C]DTBZ and [^{11}C]RAC, respectively. (**j**) 5-HT content was unaltered in the striata of control (n= 6) and VMAT2 KD (n= 9) rats. Data are shown as boxplot with the median value (central mark),

1166 the mean value (plus sign), interquartile range (boxes edges), and the extreme points of the distribution
1167 (whiskers). $^{+}P < 0.05$, $^{*}P < 0.01$. GFP, green fluorescent protein; HA-tag, hemagglutinin tag; KD, knockdown;
1168 TH, tyrosine hydroxylase; SN, substantia nigra; STR, striatum; [^{11}C]RAC, [^{11}C]raclopride; DA, dopamine; 5-
1169 HT, serotonin. Metabolites' and neurotransmitters' striatal content is reported in Table 3. Illustrations in the
1170 figure were created with BioRender.com.

1171

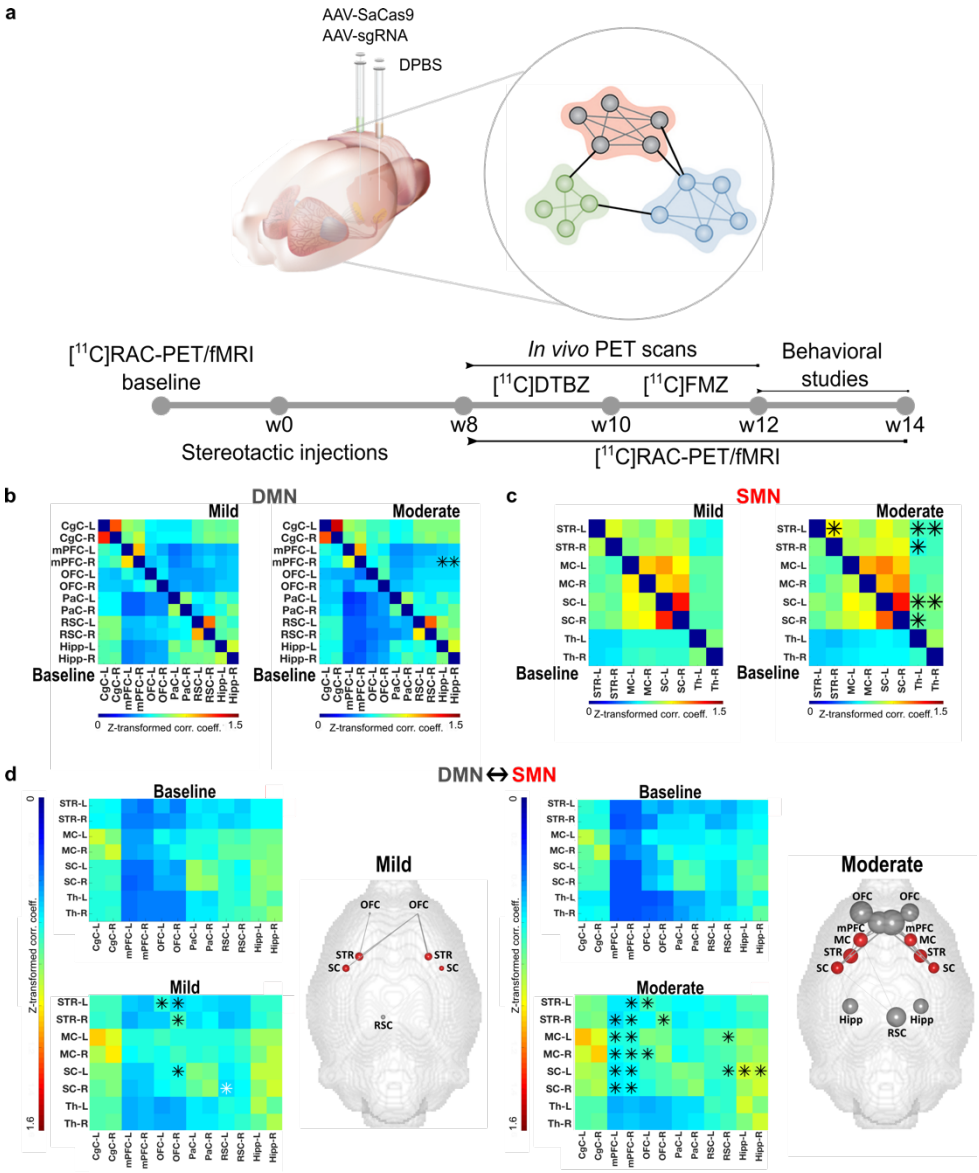

Fig. 5 Increased resting-state functional connectivity after CRISPR/SaCas9-induced VMAT2 knockdown. (**a**) Schematic illustration of the experimental design. Group level correlation matrices of the DMN (**b**) and SMN (**c**) at baseline and after CRISPR/SaCas9-targeting for rats with a *mild* (left panel) and *moderate* (right panel) VMAT2 KD. In the *moderate* KD group rs-FC was increased between the right mPFC and right and left Hipp in the DMN (**b**) and between the contralateral SC and right and left Th, as well as between the left STR and right and left Th, in the SMN (**c**). (**d**) Internetwork rs-FC changes in the *mild* KD group indicated increased rs-FC between anterior regions of the DMN and the SMN (between the left OFC and STR, and between the right OFC and the left SC, and the right and left STR). Conversely, rs-FC was decreased between regions of the posterior DMN and the SMN (between the left RSC and right SC). In the *moderate* KD group, DMN-SMN rs-FC was increased. Brain graphs, right to the matrices, illustrate the nodes and edges (raw values) that demonstrated rs-FC changes to baseline (%). *P< 0.01. *Mild*: Δ [^{11}C]DTBZ binding < 20%, n= 13; *Moderate*: Δ [^{11}C]DTBZ binding ≥ 20%, n= 10. KD, knockdown; DMN, default-mode network; SMN, sensorimotor network. mPFC, medial prefrontal cortex; Hipp, hippocampus; SC, somatosensory cortex; Th, thalamus; STR, striatum; OFC, orbitofrontal cortex; RSC, retrosplenial cortex. Abbreviations of brain regions considered for the analysis of the fMRI data, including their respective volumes, are reported in Table 2.

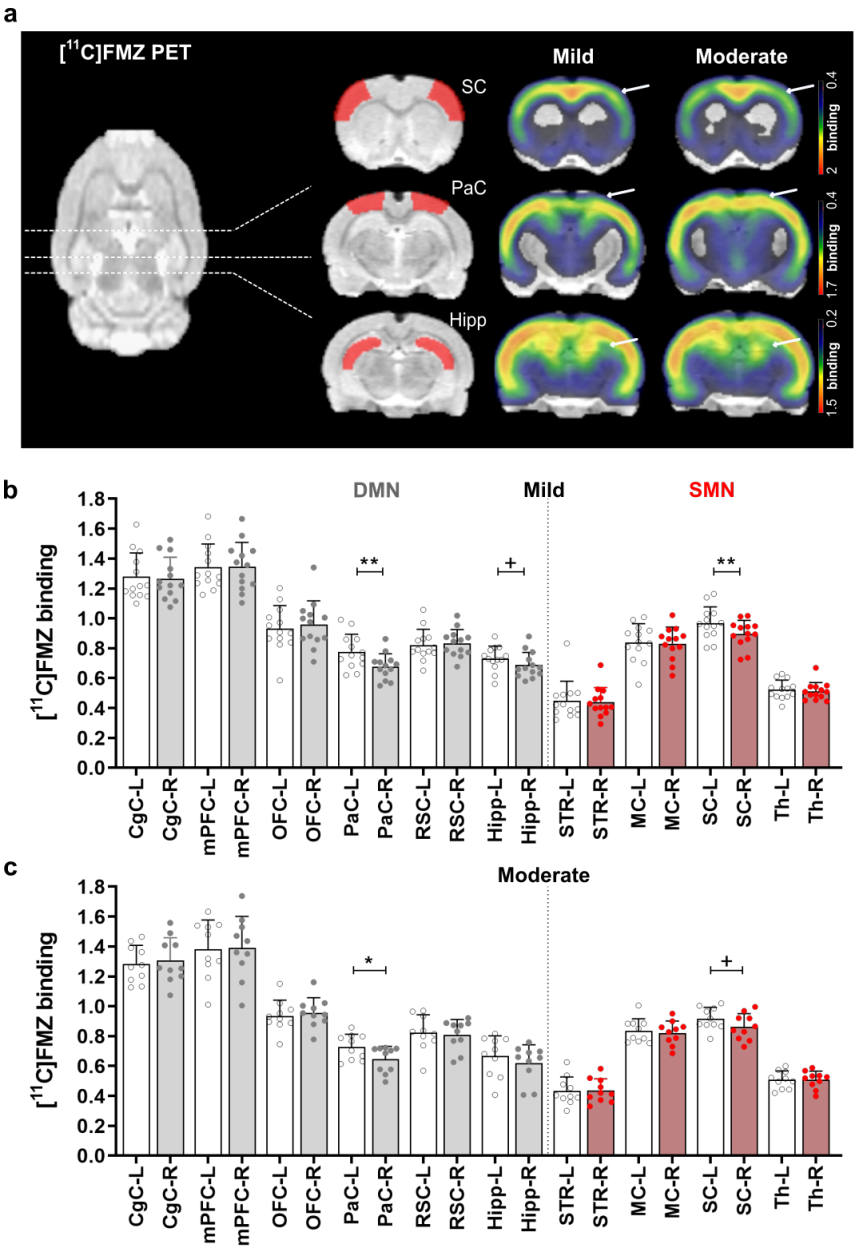

Fig. 6 CRISPR/SaCas9-induced VMAT2 knockdown alters GABA signaling. (**a**) [^{11}C]FMZ mean binding potential maps of *mild* and *moderate* VMAT2 KD rats co-registered to a rat brain atlas. Arrows and ROIs in coronal sections indicate brain regions of the DMN and SMN with altered [^{11}C]FMZ binding. [^{11}C]FMZ binding potentials from VOI-based analysis in DMN and SMN regions of rats with *mild* (**b**) and *moderate* (**c**) VMAT2 KD. [^{11}C]FMZ binding was decreased in the right PaC, SC, and Hipp of *mild* KD rats (**b**) and right PaC and SC of *moderate* KD rats (**c**). $^{+}P < 0.05$, $^{*}P < 0.01$, $^{**}P < 0.001$, Bonferroni-Sidak corrected. Data are shown as mean ± SD. *Mild*: Δ [^{11}C]DTBZ binding < 20%, n= 13; *Moderate*: Δ [^{11}C]DTBZ binding ≥ 20%, n= 10. KD, knockdown; [^{11}C]FMZ, [^{11}C]flumazenil; DMN, default-mode network; SMN, sensorimotor network. PaC, parietal cortex; Hipp, hippocampus; SC; somatosensory cortex. Abbreviations of brain regions, including their respective volumes, are reported in Table 2.

1202 **Supplementary Figures**

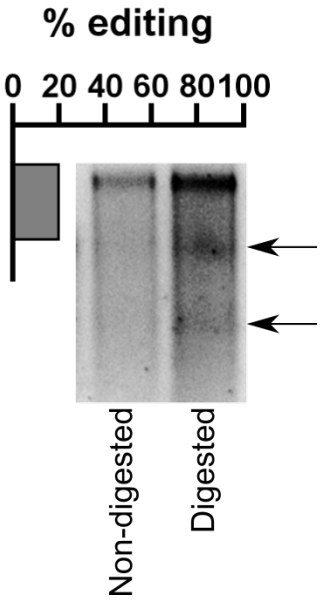

1203

1204 **Supplementary Fig. 1 *In vitro* validation of CRISPR/SaCas9-induced VMAT2 knockdown in rat primary**
1205 **cortical neurons.** One-week post-transduction with conditional vectors for SaCas9 and sgRNA-*Slc18a2*,
1206 neurons were processed for the Surveyor assay. The expected cleavage products (arrows), and estimated
1207 editing of 20%, could be seen for the digested DNA.

1208

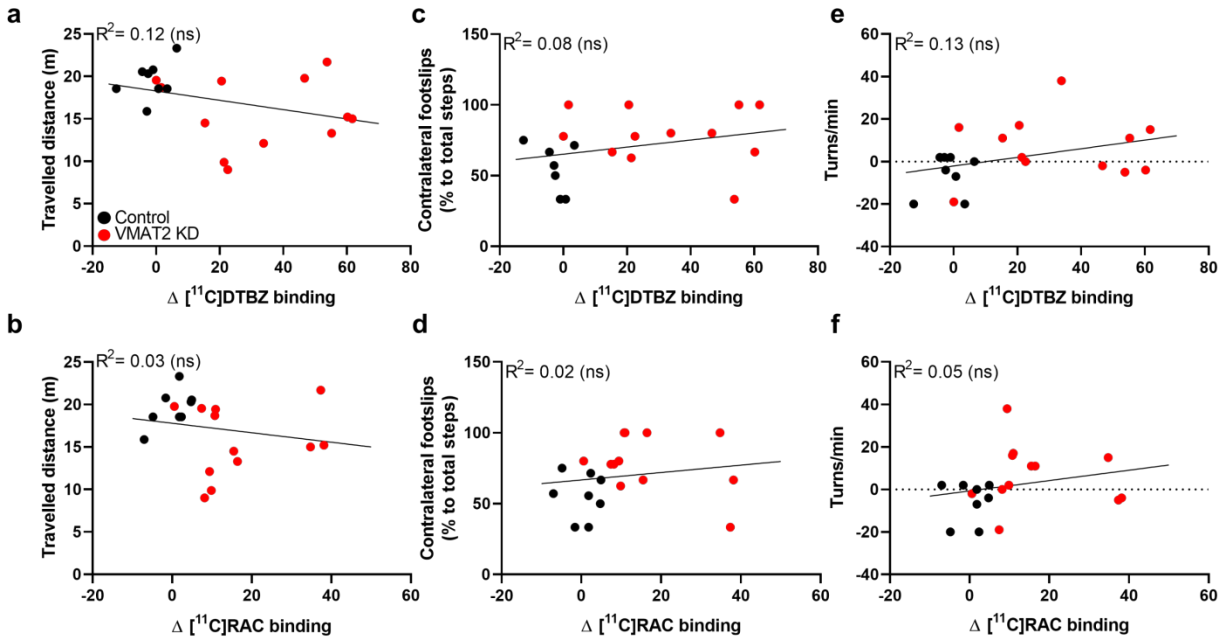

Supplementary Fig. 2 CRISPR/SaCas9-induced VMAT2 knockdown, postsynaptic changes, and motor impairment do not correlate for whole-body movements. No correlation was observed between locomotor activity and (**a**) VMAT2 expression changes (Δ [^{11}C]DTBZ binding), or (**b**) dopamine availability (Δ [^{11}C]RAC binding). The number of contralateral footslips in the beam walk test did not correlate with (**c**) changes in VMAT2 expression (Δ [^{11}C]DTBZ binding) or (**d**) dopamine availability (Δ [^{11}C]RAC binding). Spontaneous rotations did not correlate with (**e**) changes in VMAT2 expression (Δ [^{11}C]DTBZ binding) or (**f**) dopamine availability (Δ [^{11}C]RAC binding). ns $P \geq 0.05$. Control rats n= 8; VMAT2 KD rats n= 12. KD, knockdown; [^{11}C]RAC, [^{11}C]raclopride.

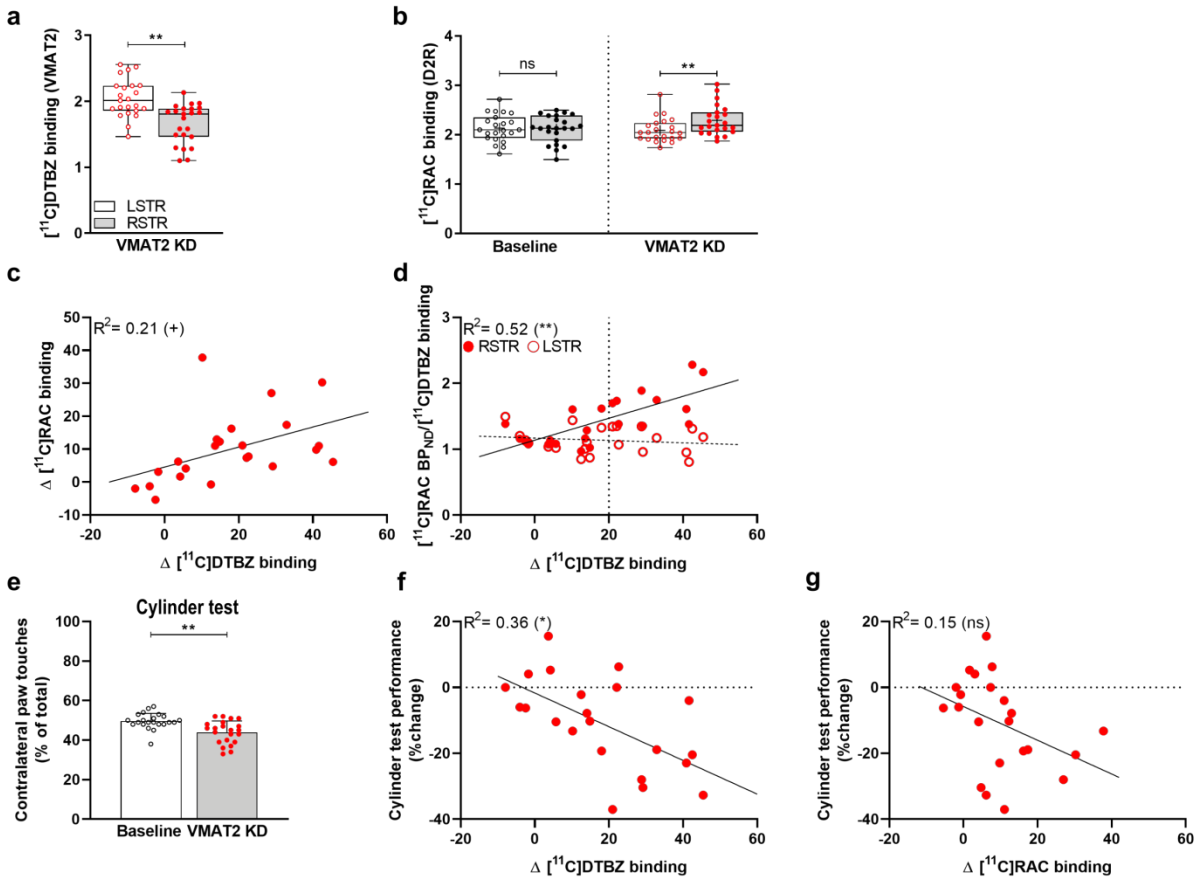

Supplementary Fig. 3 Reproducibility of the CRISPR/SaCas9-induced VMAT2 knockdown. (**a**) [^{11}C]DTBZ in VMAT2 KD rats and (**b**) [^{11}C]RAC PET at baseline and after CRISPR/SaCas9-induced VMAT2 KD. (**c**) A strong correlation between Δ [^{11}C]RAC and Δ [^{11}C]DTBZ binding is shown. (**d**) At 20% VMAT2 KD (Δ [^{11}C]DTBZ binding), D2R binding (Δ [^{11}C]RAC binding) prominently increased. This threshold was therefore set to separate the rats into *mild* and *moderate*. Data are shown as boxplot with the median value (central mark), the mean value (plus sign), interquartile range (boxes edges), and the extreme points of the distribution (whiskers). Baseline n= 23, VMAT2 KD n= 23. (**e**) Cylinder test at baseline (n= 22) and 12 - 14 weeks after CRISPR/SaCas9 gene-editing (n= 22). VMAT2 KD rats showed reduced contralateral paw touches compared to baseline. Rats performance in the cylinder test, % change from baseline, correlated with reduced VMAT2 expression (Δ [^{11}C]DTBZ binding) (**f**), but not with dopamine availability (Δ [^{11}C]RAC binding) (**g**). Data are shown as mean ± SD. $^{+}P< 0.05$, $^{*}P< 0.01$, $^{**}P< 0.001$. KD, knockdown; [^{11}C]RAC, [^{11}C]raclopride.

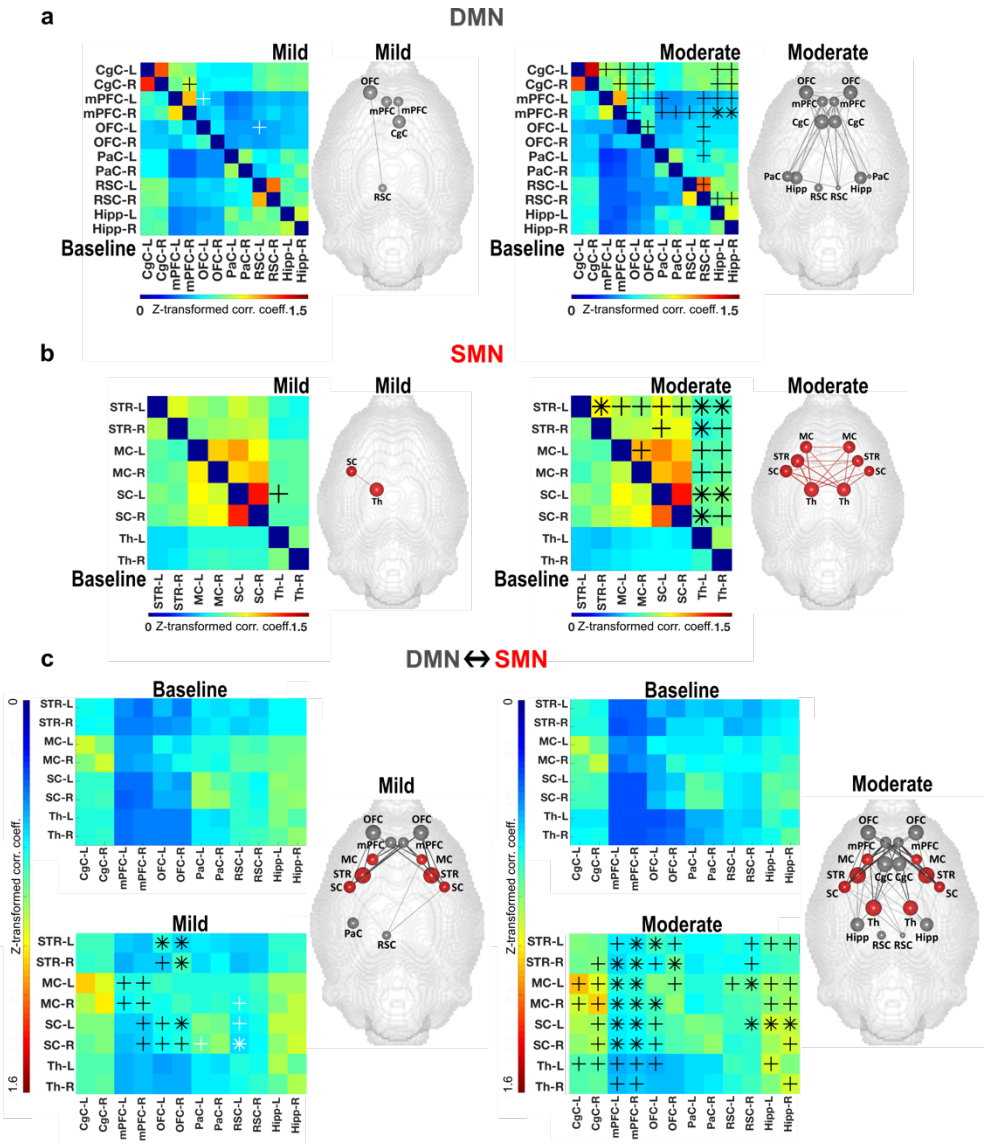

Supplementary Fig. 4 Increased resting-state functional connectivity after CRISPR/SaCas9-induced VMAT2 knockdown. Group level correlation matrices of the DMN (**a**) and SMN (**b**) at baseline and after VMAT2 KD for *mild* (left panel) and *moderate* (right panel) rats. Brain graphs, right to the matrices, illustrate the nodes and edges (raw values) that demonstrated rs-FC changes to baseline (%) in DMN (**a**) and SMN (**b**). (**a**) In rats with *mild* VMAT2 KD, we observed divergent rs-FC changes to baseline in regions of the anterior DMN (left mPFC and OFC, right mPFC and CgC). In rats with *moderate* VMAT2 KD, we observed rs-FC increase in most regions of the anterior DMN, extending to the posterior DMN (RSC bilaterally, right RSC, and Hipp bilaterally). (**b**) In rats with *mild* VMAT2 KD, we observed rs-FC increase between the contralateral SC and Th, which intensified in *moderate* VMAT2 KD rats and extended to most of the regions of the SMN. (**c**) Group level correlation matrices of the DMN-SMN rs-FC changes at baseline and after VMAT2 KD for *mild* (left panel) and *moderate* (right panel) rats. Brain graphs, right to the matrices, illustrate the nodes and edges (raw values) that demonstrated internetwork rs-FC changes to baseline (%). Internetwork FC changes in rats with *mild* VMAT2 KD indicated increased rs-FC between anterior regions of the DMN and the SMN (between OFC and STR, SC bilaterally, between right mPFC and MC, SC bilaterally), and decreased rs-FC between posterior regions of the DMN and the SMN (between left RSC and right MC, and SC bilaterally). Increased DMN-SMN rs-FC was found in rats with *moderate* VMAT2 KD. Internetwork

1250 rs-FC alterations extended between CgC/Hipp, and SC, MC, Th. $^{+}P < 0.05$, $^{*}P < 0.01$. *Mild*: Δ [^{11}C]DTBZ
1251 binding < 20%, n= 13; *Moderate*: Δ [^{11}C]DTBZ binding ≥ 20%, n= 10. KD, knockdown; DMN, default-mode
1252 network; SMN, sensorimotor network. mPFC, medial prefrontal cortex; OFC, orbitofrontal cortex; CgC,
1253 cingulate cortex; RSC, retrosplenial cortex; Hipp, hippocampus; SC, somatosensory cortex; Th, thalamus;
1254 STR, striatum; MC, motor cortex. Abbreviations of brain regions considered for the analysis of the fMRI data,
1255 including their respective volumes, are reported in Table 2.

1256

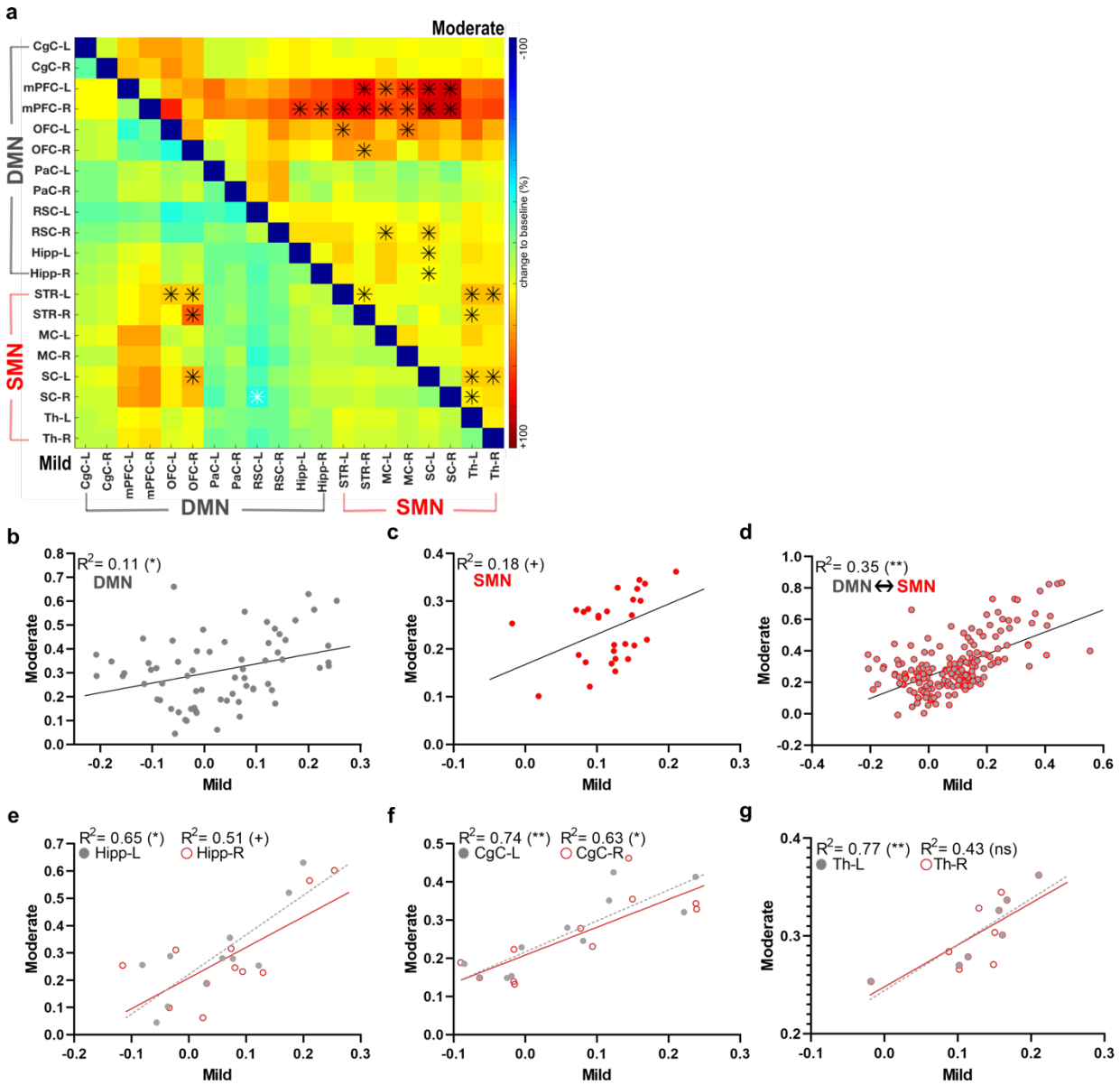

Supplementary Fig. 5 Node correlation analyses evidence pattern similarity and a linear relationship between the magnitude of the resting-state functional connectivity changes in *mild* and *moderate* rats. (**a**) Group level correlation matrices of the intraregional and internetwork rs-FC changes to baseline (%) for *mild* and *moderate* VMAT2 KD rats. (**b-d**) Group level intraregional and internetwork rs-FC changes correlated linearly between the two groups. Node correlation analysis between *mild* and *moderate* VMAT2 KD rats indicated a linear increase in the magnitude of the rs-FC changes to baseline in the right and left Hipp (**e**), and CgC (**f**). (**g**) Rs-FC changes (%) in the SMN correlated linearly between *mild* and *moderate* VMAT2 KD rats in the left, but not in the right Th. Our data suggest a similarity in the pattern of the intraregional and internetwork rs-FC changes between rats with *mild* and *moderate* VMAT2 KD and a linear relationship between the magnitude of the rs-FC changes. $^{+}P < 0.05$, $^{*}P < 0.01$, $^{**}P < 0.001$. *Mild*: Δ [^{11}C]DTBZ binding < 20%, n= 13; *Moderate*: Δ [^{11}C]DTBZ binding ≥ 20%, n= 10. KD, knockdown; DMN, default-mode network; SMN, sensorimotor network. Hipp, hippocampus; CgC, cingulate cortex. Th, thalamus. Abbreviations of brain regions considered for the analysis of the fMRI data, including their respective volumes, are reported in Table 2.

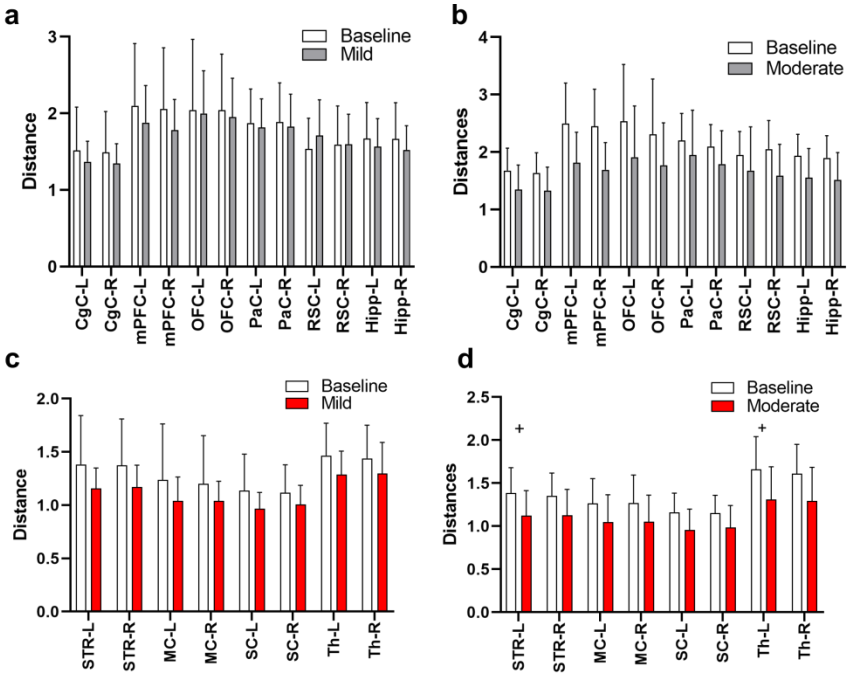

1272

1273 **Supplementary Fig. 6 Graph theoretical analyses reveal lateralized recruitment of SMN regions**
1274 **following the CRISPR/SaCas9-induced VMAT2 *moderate* knockdown.** Quantitative graph theoretical
1275 analyses of the global mean connection distance indicated no changes for *mild* (**a**) and *moderate* (**b**) VMAT2
1276 KD rats in the DMN. (**c**) Rats with *mild* VMAT2 KD displayed no changes in the SMN. (**d**) Instead, rats with
1277 *moderate* VMAT2 KD presented shorter functional paths to the nodes in the contralateral Th and STR. Data
1278 are shown as mean ± SD. $^{+}P < 0.05$, Bonferroni-Sidak-corrected. *Mild*: Δ [^{11}C]DTBZ binding < 20%, n= 13;
1279 *Moderate*: Δ [^{11}C]DTBZ binding ≥ 20%, n= 10. KD, knockdown; DMN: default-mode network, SMN:
1280 sensorimotor network; Th: Thalamus; STR: striatum. Abbreviations of brain regions considered for the
1281 analysis of the fMRI data, including their respective volumes, are reported in Table 2.

1282

1283 ## Tables

1284 **Table 1: sgRNAs sequences.**

1285

1286

1287

SgRNAs	DNA Target Sequences 5'- 3'	PAM (NNGRRT) 5'- 3'
Slc18a2	CGATGAACAGGATCAGTTTGC	GCGAGT
lacZ	CCTTCCCAACAGTTGCGCAGC	CTGAAT

1288

1289

1290

1291

1292

1293

1294

1295

1296

1297

1298 **Table 2: Brain regions included in the Paxinos rat brain atlas, including their respective volumes**
1299 **and abbreviations.**

Brain region (ROI)	Hemisphere	ROI volume [mm^3]	Abbreviation
Striatum	left	43.552	STR
	right		
Cingulate Cortex	left	14.480	CgC
	right		
Medial Prefrontal Cortex	left	6.304	mPFC
	right		
Motor Cortex	left	32.608	MC
	right		
Orbitofrontal Cortex	left	18.936	OFC
	right		
Parietal Cortex	left	7.632	PaC
	right		
Retrosplenial Cortex	left	18.920	RSC
	right		
Somatosensory Cortex	left	71.600	SC
	right		
Hippocampus	left	25.064	Hipp
	right		
Thalamus	left	30.712	Th
	right		

1300

1301 **Table 3: Dopamine, 3,4-Dihydroxyphenylacetic acid (DOPAC), homovanillic acid (HVA), and**
1302 **serotonin (5-HT) striatal content (nmol/mg) determined by HPLC.**

Neurotransmitter or Metabolite	nmol/mg (mean ± SD)	
DA	**Control**	**VMAT2 KD**
STR-L	244 ± 109	351 ± 168
STR-R	308 ± 166	100 ± 97
DOPAC	**Control**	**VMAT2 KD**
STR-L	34 ± 7	34 ± 11
STR-R	38 ± 4	27 ± 5
HVA	**Control**	**VMAT2 KD**
STR-L	24 ± 5	25 ± 5
STR-R	26 ± 6	19 ± 4
5-HT	**Control**	**VMAT2 KD**
STR-L	17 ± 2	19 ± 8
STR-R	19 ± 6	23 ± 9

1303

1304

Supplementary Tables

Supplementary Table 1: *P* values of the functional connectivity changes in regions of the DMN for rats with *mild* VMAT2 knockdown. Data were analyzed using paired t-tests.

Mild	**Hipp-R**	**Hipp-L**	**RSC-R**	**RSC-L**	**PaC-R**	**PaC-L**	**OFC-R**	**OFC-L**	**mPFC-R**	**mPFC-L**	**CgC-R**
CgC-L	0.40	0.56	0.95	0.33	0.76	0.84	0.22	0.27	0.07	0.07	0.61
CgC-R	0.30	0.41	0.83	0.29	0.84	0.86	0.17	0.23	0.03	0.08	
mPFC-L	0.21	0.34	0.77	0.73	0.36	0.55	0.46	0.02	0.53		
mPFC-R	0.12	0.23	0.54	0.99	0.24	0.46	0.24	0.61			
OFC-L	0.49	0.55	0.20	0.05	0.51	0.67	0.18				
OFC-R	0.31	0.20	0.26	0.13	0.23	0.45					
PaC-L	0.61	0.39	0.84	0.08	0.31						
PaC-R	0.74	0.59	0.83	0.11							
RSC-L	0.18	0.22	0.31								
RSC-R	0.75	0.65									
Hipp-L	0.67										

Supplementary Table 2: *P* values of the functional connectivity changes in regions of the DMN for rats with *moderate* VMAT2 knockdown. Data were analyzed using paired t-tests.

Moderate	**Hipp-R**	**Hipp-L**	**RSC-R**	**RSC-L**	**PaC-R**	**PaC-L**	**OFC-R**	**OFC-L**	**mPFC-R**	**mPFC-L**	**CgC-R**
CgC-L	0.05	0.02	0.07	0.11	0.24	0.22	0.05	0.03	0.03	0.04	0.07
CgC-R	0.03	0.02	0.08	0.14	0.21	0.25	0.04	0.01	0.03	0.05	
mPFC-L	0.01	0.03	0.03	0.09	0.05	0.04	0.04	0.04	0.06		
mPFC-R	**0.005**	**0.007**	0.01	0.03	0.03	0.03	0.06	0.01			
OFC-L	0.08	0.10	0.04	0.13	0.24	0.21	0.05				
OFC-R	0.16	0.11	0.03	0.07	0.29	0.47					
PaC-L	0.35	0.60	0.03	0.10	0.13						
PaC-R	0.42	0.32	0.06	0.22							
RSC-L	0.10	0.07	0.02								
RSC-R	0.03	0.04									
Hipp-L	0.15										

1337 **Supplementary Table 3: *P* values of the functional connectivity changes in regions of the SMN for**
1338 **rats with *mild* VMAT2 knockdown. Data were analyzed using paired t-tests.**
1339

Mild	Th-R	Th-L	SC-R	SC-L	MC-R	MC-L	STR-R
STR-L	0.13	0.06	0.21	0.14	0.23	0.21	0.39
STR-R	0.13	0.09	0.19	0.13	0.39	0.29	
MC-L	0.24	0.16	0.47	0.16	0.46		
MC-R	0.29	0.23	0.38	0.21			
SC-L	0.14	0.04	0.76				
SC-R	0.30	0.12					
Th-L	0.79						
Th-R							

1340
1341 **Supplementary Table 4: *P* values of the functional connectivity changes in regions of the SMN for**
1342 **rats with *moderate* VMAT2 knockdown. Data were analyzed using paired t-tests.**
1343

Moderate	Th-R	Th-L	SC-R	SC-L	MC-R	MC-L	STR-R
STR-L	**0.01**	**0.004**	0.02	0.05	0.03	0.04	**0.007**
STR-R	0.02	**0.008**	0.06	0.04	0.16	0.07	
MC-L	0.04	0.01	0.10	0.08	0.04		
MC-R	0.02	0.02	0.07				
SC-L	**0.003**	**0.001**	0.11				
SC-R	0.02	**0.008**					
Th-L	0.07						
Th-R							

1344
1345 **Supplementary Table 5: *P* values of the functional connectivity internetwork changes in regions of**
1346 **the DMN and SMN for rats with *mild* VMAT2 knockdown. Data were analyzed using paired t-tests.**
1347

Mild	Hipp-R	Hipp-L	RSC-R	RSC-L	PaC-R	PaC-L	OFC-R	OFC-L	mPFC-R	mPFC-L	CgC-R	CgC-L
STR-L	0.23	0.18	0.82	0.26	0.94	0.93	**0.006**	**0.005**	0.10	0.15	0.27	0.29
STR-R	0.16	0.44	0.65	0.32	0.65	0.98	**0.0004**	0.03	0.06	0.19	0.24	0.31
MC-L	0.34	0.39	0.92	0.29	0.93	0.94	0.11	0.40	0.02	0.04	0.10	0.07
MC-R	0.26	0.60	0.18	0.04	0.49	0.88	0.37	0.16	0.02	0.05	0.18	0.35
SC-L	0.12	0.26	0.78	0.05	0.87	0.46	**0.002**	0.02	0.03	0.05	0.13	0.17
SC-R	0.13	0.57	0.19	**0.006**	0.89	0.04	0.01	0.04	0.02	0.06	0.18	0.28
Th-L	0.35	0.27	0.55	0.39	1.00	0.89	0.09	0.21	0.11	0.17	0.14	0.17
Th-R	0.38	0.98	0.66	0.26	0.94	0.70	0.09	0.15	0.09	0.11	0.28	0.33

1348
1349

1350 **Supplementary Table 6: *P* values of the functional connectivity internetwork changes in regions of**
1351 **the DMN and SMN for rats with *moderate* VMAT2 knockdown. Data were analyzed using paired t-**
1352 **tests.**
1353

Moderate	**Hipp-R**	**Hipp-L**	**RSC-R**	**RSC-L**	**PaC-R**	**PaC-L**	**OFC-R**	**OFC-L**	**mPFC-R**	**mPFC-L**	**CgC-R**	**CgC-L**
STR-L	0.02	0.02	0.02	0.11	0.16	0.30	0.03	**0.003**	**0.006**	0.01	0.07	0.09
STR-R	0.08	0.08	0.04	0.14	0.30	0.63	**0.008**	0.01	**0.002**	**0.003**	0.04	0.07
MC-L	0.03	0.03	**0.003**	0.03	0.45	0.46	0.04	0.07	**0.003**	**0.003**	0.02	0.02
MC-R	0.03	0.05	0.05	0.18	0.52	0.97	0.19	**0.008**	**0.01**	**0.007**	0.03	0.03
SC-L	**0.004**	**0.008**	**0.008**	0.08	0.11	0.44	0.05	0.02	**0.003**	**0.004**	0.04	0.06
SC-R	0.02	0.08	0.06	0.35	0.27	0.94	0.07	0.04	**0.001**	**0.003**	0.04	0.07
Th-L	0.06	0.02	0.09	0.10	0.17	0.15	0.06	0.03	0.02	0.03	0.03	0.04
Th-R	0.03	0.10	0.09	0.23	0.15	0.13	0.14	0.08	0.02	0.04	0.07	0.15

1354
1355 **Supplementary Table 7: Bonferroni-Sidak corrected *P* values for graph theoretical measures of the**
1356 **global mean connection distance in *mild* and *moderate* VMAT2 knockdown rats. Data were analyzed**
1357 **using paired t-tests.**
1358

Region	***Mild***	***Moderate***
CgC-L	0.39	0.48
CgC-R	0.37	0.45
mPFC-L	0.41	0.24
mPFC-R	0.28	0.10
OFC-L	0.87	0.81
OFC-R	0.67	0.89
PaC-L	0.68	0.96
PaC-R	0.66	0.83
RSC-L	0.18	0.96
RSC-R	0.97	0.38
Hipp-L	0.50	0.42
Hipp-R	0.34	0.35
STR-L	0.15	**0.01**
STR-R	0.18	0.09
MC-L	0.27	0.64
MC-R	0.29	0.48
SC-L	0.16	0.08
SC-R	0.29	0.35
Th-L	0.12	**0.03**
Th-R	0.28	0.09

1359
1360

1361 **Supplementary Table 8: Primers used to amplify the *Slc18a2* and the *lacZ* loci in the Surveyor assay**
1362 **and DNA expected fragments sizes.**

SgRNAs	Forward Primer 5'- 3'	Reverse Primer 5'- 3'	Fragment size (bp)
Slc18a2	CTTGGGGATCCTCTAAGGCAG	TACAGCGCGGTTCTTCAACT	313_280
lacZ	GTCGTGACTGGGAAAACCCT	TTGTTCCCACGGAGAATCCG	200_80

1363
1364 **Supplementary Table 9: [^{11}C]DTBZ, [^{11}C]methylphenidate, [^{11}C]raclopride and [^{18}F]GE-180 injected**
1365 **and molar activities.**
1366

Radioligand	Injected Activity (Mean ± SD) MBq	Molar Activity (Mean ± SD) GBq/µmol
[^{11}C]DTBZ	25 ± 1	93 ± 35
[^{11}C]MP	25 ± 1	57 ± 14
[^{11}C]RAC	25 ± 1	88 ± 41
[^{18}F]GE-180	24 ± 3	576 ± 283

1374
1375
1376 **Supplementary Table 10: [^{11}C]raclopride, [^{11}C]DTBZ, [^{11}C]flumazenil injected and molar activities.**

1377

Radioligand	Injected Activity (Mean ± SD) MBq	Molar Activity (Mean ± SD) GBq/µmol
[^{11}C]RAC t0	27 ± 4	108 ± 49
[^{11}C]RAC t8	28 ± 1	115 ± 41
[^{11}C]DTBZ	27 ± 1	180 ± 48
[^{11}C]FMZ	27 ± 1	109 ± 40